



Research Article

Novel bioluminescent oceanic optimization with explainable AI for accurate skin cancer diagnosis and enhanced dermatologist support

Mudassir Khan^{a,*}, Sai Bhuvana Kurada^b, Alaa Mohammad Menshawi^c, Varun Malik^d, Meteb M. Altaf^e

^aDepartment of Computer Science, College of Computer Science, Applied College Tanumah, King Khalid University, Abha, Saudi Arabia

^bArizona State University, Tempe, Arizona, 85281, United States

^cInformation Systems department, College of Computer and Information Sciences, Imam Mohammad Ibn Saud Islamic University (IMSIU), Riyadh, Kingdom of Saudi Arabia

^dChitkara University Institute of Engineering and Technology, Chitkara University, Rajpura, India

^eDisability Research Institute, Health Sector, King Abdulaziz City for Science and Technology, Riyadh, Kingdom of Saudi Arabia

ARTICLE INFO

Keywords:

Bioluminescent oceanic optimization
Decoder
Dermatologist
Encoder
Explainable AI
Skin cancer
Skin cancer diagnosis

ABSTRACT

Skin cancer poses a significant global health threat, where timely and accurate diagnosis is crucial for improving patient outcomes. Although deep learning methods have demonstrated considerable success in dermatological image analysis, their black-box nature limits clinical adoption due to a lack of transparency and interpretability. To overcome this difficulty, it is suggested that an explainable artificial intelligence (XAI) framework can be applied using an optimal encoder-decoder architecture, which enhances the accuracy of dermatology-specific skin cancer diagnostics and offers better assistance to dermatologists. The specified model is tested on the benchmark dermoscopic image datasets, such as the ISIC archive and the HAM10000. To extract rich and hierarchical features of skin lesion images, the encoder uses pre-trained backbones, which are ResNet-50 and EfficientNet-B4. It uses a tailored decoder, based on U-Net and SegNet design, to recover lesion segmentation maps and give multi-class lesions classification. Nature-based novel bioluminescent oceanic optimization (BOO) algorithm is proposed to be used in feature selection, which determines the most significant features. A squeeze attention network (SAttNet) emphasizes features around the edges of lesions, thus narrowing the scope of the model and enhancing the accuracy of the diagnosis. Explainability is achieved through a multi-level post-hoc strategy: Gradient-weighted Class Activation Mapping (Grad-CAM) highlights critical regions within the encoder's feature maps; SHapley Additive explanations (SHAP) quantifies the contribution of individual features to the prediction; and local interpretable model-agnostic explanations (LIME) generates localized, human-understandable explanations for diagnostic output. The results show outstanding performance, achieved classification accuracies of 99.956% and 99.644% on the ISIC and HAM10000 datasets, respectively.

1. Introduction

One of the most frequent cancers globally, skin cancer has been growing consistently for decades (Verma, N. *et al.* 2025). Skin cancer was formerly identified by clinical examination and histological biopsy, which were successful but invasive and time-consuming (Qadrie, Z. *et al.* 2025, Evans, H. *et al.* 2025). Dermoscopy and imaging advances have made non-invasive skin cancer screening easier. Manual clinical evaluation and histological investigation are time-consuming and prone to inter-observer unpredictability for skin cancer diagnosis (Rashid, M., and Sharma, M. 2025). Classical machine learning (ML) classifiers like support vector machines (SVM), K-nearest neighbors (k-NN), and decision tree replaced manual feature extraction approaches like color, texture, and form descriptors in early computer-aided diagnosis models (Ronchetti, M., and Simeonov, A., 2025). However, these models required manual feature selection and engineering, which is laborious and inefficient. Lots of the traditional models are unable to reflect the complex tendencies in dermoscopic images distinguishing between malignant and benign skin lesions (Verma, A. and Kaur, P., 2025).

However, it is still important to be familiar with these traditional methods since they are still in use in some of the clinical settings and as benchmark standards. Accurate diagnosis may lead to timely surgical removal, thus resolving morbidity and healthcare costs. Diagnostic errors, on the other hand, lead to unnecessary biopsies or malignancies that would not have been detected, thus undermining the patient's trust and health outcomes (Noor, A. A. *et al.* 2025). The early detection allows custom therapy and management of patients, which allows medical organizations to manage their resources more effectively and decrease the anxiety of patients due to faster and reliable results. Automated image processing and high-throughput screening have revolutionized skin cancer diagnosis with AI. Deep learning (DL) models are AlexNet, VGG, ResNet, DenseNet, and Inception, which learn hierarchical features from raw images (Abbas, S. *et al.* 2025). Explainable artificial intelligence (XAI) gives interpretable insights to improve dermatological support and patient care, filling this gap. XAI is a crucial innovation to overcome the black box problem of many AI models, including DL based skin cancer diagnostic systems. SHapley Additive explanations (SHAP), Gradient-weighted Class Activation Mapping (Grad-CAM),

*Corresponding author:

E-mail address: mkmijob@kku.edu.sa (M Khan)

Received: 14 July, 2025 Accepted: 15 December, 2025 Epub Ahead of Print: 19 February 2026 Published: 24 February, 2026

DOI: 10.25259/JKSUS_1183_2025

and attention processes highlight key characteristics or areas in skin lesion images for visual and quantitative explanations (Ennab, M., and Mccheick, H., 2025; Shoughi, A. et al., 2025). This study presents an XAI with an optimized encoder–decoder for accurate skin cancer diagnosis, which strengthens clinical decision-making and dermatologist support.

The next part of this manuscript is outlined as follows. Section 2 reviews the related literature, while Section 3 expounds the materials and methods, of which data acquisition, preprocessing, encoder and decoder architectures, and the feature selection procedures are detailed. The results and resultant discussion are presented in sections 4 and 5, respectively. The manuscript climaxes in Section 6.

2. Related Work

2.1 Machine learning and deep learning techniques

The parallel convolutional spiking neural network (PCSN-Net) (Kumar, K. A. and Vanmathi, C. 2025) is used for efficient skin cancer diagnosis. Achieving 95.7% accuracy, 94.7% sensitivity, and 92.6% specificity, PCSN-Net demonstrated strong diagnostic performance. Fully convolutional deep supervised convolutional neural network (FCDS-CNN) model (Nawaz, K. et al. 2025) optimized for early melanoma detection. It reached an average accuracy of 96% in seven classes by using class weighting and data augmentation, which improved the work with imbalanced datasets. A convolutional neural network is prioritized, and the region-based convolutional neural network (R-CNN) algorithm is employed to find minor changes in skin lesions (Kavitha, C. et al. 2024). A CNN-based classification system (Vibha, T. R. et al. 2025, Reddy, A. S. and MP, G. 2025) have suggested a dual-component model based on the proposed segmentation using optimized Mask R-CNN and the GEMLO model, where the optimal feature selection is based on the framework. Hybrid architecture uses InceptionV3 and DenseNet121 as feature extractors, and then fuses the resultant representations with weighted sum rule is based on that (Akter, M. et al. 2025). This was improved by adopted a heterogeneous ensemble learning model that was based on stacked support vectors machines (Das, A. and Mohanty, M. N. 2025). A multimodal model, which combines dermoscopic images with synthetically generated clinical notes, with the help of GPT-4-turbo and the Align Before Fuse (ALBEF) framework (Chakkarapani, V. et al. 2025). A lightweight melanoma screening approach which combined Gaussian filtering, deep learning–based nonlinear data processing (DLNDP) feature extractor, and hybrid randomized adaptive neuro-fuzzy inference system (RANFyIS) detection model (Sargunan, I. et al. 2025), achieving 90.42% accuracy with a high true positive rate of 92.46%. The same architecture and confirmed reliability with consistent metrics, reinforcing potential for non-invasive and rapid melanoma screening in clinical settings (Swapno, S. M. R. et al. 2025).

2.2 Explainable AI in skin disease

Meta-explainable privacy-preserving federated learning (Meta-XPFL) framework is used for skin cancer diagnosis using IoMT images. XAI provided interpretability, addressing clinical usability (Serhani, M. A. et al. 2025). IARS SegNet, a lesion segmentation network based on SegNet with residual convolution and global attention (Narayanan, V. S. et al. 2024). YOLOv8 is used for Region of interest (ROI) detection, enabling better lesion localization and focus before classification (AbuAlkesh, H. et al. 2025). A hybrid model integrates ViT, a custom CNN, and Xception, supported by Grad-CAM for visual explanation (Ali, A. et al. 2025). However, reliance solely on visual features restricted the inclusion of other modalities specific knowledge. Synthetic minority over-sampling technique (SMOTE) is used for class balancing and used CNN and ResNet50 for feature extraction, along with LIME for local interpretability (Gupta, R. K., 2025). To fill this gap, a Trustworthiness Index for XAI using EfficientNet-B0 (Ieracitano, C. et al. 2025). Modified UNet-inspired encoder-decoder architecture is preserved spatial features for precise melanoma segmentation (Kibriya, H. et al. 2025). To bridged this gap by assessing XAI through eye-tracking in clinical setting (Chanda, T. et al. 2025). The model transparency by comparing CNN, Xception, EfficientNet, VGG, and ResNet using XAI techniques like

LIME and Grad-CAM across skin cancer, brain tumor, and pneumonia detection (Garg, P. et al. 2025). The concept of explainable diagnosis by MpoX-XDE, a hybrid deep model combining Xception, DenseNet201, and EfficientNetB7 (Kumar Saha, D. et al. 2025) for multi-disease classification, monkey pox, and skin conditions. With 98.8% accuracy of Grad-CAM for visualizing predictions, the model illustrated the effectiveness of XAI not only in diagnosis.

Problem identification: From the comprehensive review (Table 1), critical research gaps in the current landscape of ML, DL, and XAI for skin disease diagnosis have been identified. These include poor performance on unbalanced datasets, lack of precise lesion boundary detection, limited clinical usability due to absence of interpretability mechanisms, restricted adaptability from single-model dependencies, weak generalization across datasets, underutilization of handcrafted domain-specific features, dependency on image-only analysis without contextual clinical data, high computational complexity unsuitable for real-time applications, and lack of transparent, explainable decision-making. In the domain of XAI-driven models either fail to deliver lesion-level segmentation, suffer from high model complexity, and lack comprehensive multi-modal fusion for richer diagnostics. Weak spatial segmentation consistency, absence of disease-specific differentiation, and scalability issues remain a problem, hence restricting its practical application in clinical settings. To fill these complex gaps, the current study offers an XAI architecture built around an optimal encoder-decoder model, a combination of the ResNet50 and EfficientNet-B4 to extract all possible features, squeeze attention network (SAttNet) to selectively locate lesions, and a hybrid decoder that is based on the U-Net and SegNet to ensure the accurate division of parts and structural arrangement. Bioluminescent oceanic optimization (BOO) algorithm is used to ensure successful feature selection whereas SHAP, LIME, and Grad-cAM are added to ensure post-hoc explainability. Such a combined model will not only enhance the accuracy of diagnosis in a wide variety of datasets, but it also leads to clinical trust due to the transparent and interpretable decision-making, which is solution to dermatologist-aided skin cancer diagnosis.

3. Materials and Methods

This section describes the methodological frameworks supporting the establishment of clinical reliability, interpretability, and accuracy for the analysis of skin cancer. The conceptual structure of the proposed skin cancer diagnostic model is shown in Fig. 1.

3.1 Data preparation and augmentation

This paper used composite of publicly accessible dermoscopic image datasets, namely ISIC last year (2018), ISIC last year (2019), ISIC last year (2020), and HAM10000 skin image datasets (Purni, J. T. and Vedhapriyavadhana, R. 2024) for the development of skin lesion classifier. The HAM10000 data set consists of 10,015 images, classified into 7 diagnostic classes: dermatofibroma (DF), melanocytic nevi (NV), melanoma (MEL), benign keratosis-like lesions (BKL), basal cell carcinoma (BCC), actinic keratoses (AKIEC), and vascular lesions (VASC). Dermoscopic images are shown in Fig. 2 for each class as a representative image. Geometric transformations, such as horizontal and vertical flips, 90 degrees and 180 degrees rotations, etc., were used as well as quality-based augmentations, such as Gaussian blur and additive Gaussian noise, as data-augmentation techniques. These operations simulate real life variations and distortions, thus increasing the robustness of the model to various inputs. All original and augmented images were processed using an improved Canny edge detector (ICED) module to highlight the lesion boundary features. The preprocessing pipeline was set up to be compatible and uniform across all input images. In order to get roughly the same input dimensions and reduce computation burden, images were automatically down sampled to 32*32 pixels. Pixel values were then normalized either in the [0, 1] or [- 1, 1] range, depending on the normalization needs of the model being trained; the normalization made training easier and increased the rate of convergence. Depending on the classification strategy used, diagnostic class labels were expressed either as one-hot vectors, or as integer encodings. After augmentation and integration of ICED, the

Table 1. Comparison of recent studies on XAI models for skin cancer diagnosis.

Ref	Focus of work	Contributions	Dataset used	Findings	Identified research gaps	Solution to address gaps
Serhani, M. A. et al. 2025	Federated skin cancer diagnosis with explainability	Meta-XPFL with SMPC and XAI;	HAM10000	Accuracy: 94.2%, high privacy	Lacks lesion-level segmentation, limits diagnostic granularity	Introduce segmentation with encoder-decoder and Grad-CAM visual explanations
Narayanan, V. S. et al. 2024	Lesion segmentation network	IARS SegNet, global attention, skip connections	ISIC 2019	Dice: 0.87, Jaccard: 0.81	No support for classification, only segmentation	Fuse with multi-class decoder for end-to-end diagnosis
AbuAlkebash, H. et al. 2025	Region-specific lesion detection & classification	YOLOv8, ViT for classification, SHAP & Grad-CAM for XAI	ISIC + Annotated ROIs	Accuracy: 93%	High complexity due to ensemble ViT and YOLOv8	Propose lightweight decoder + ViT fusion with optimized inference speed
Ali, A. et al. 2025	Hybrid DL classification model	ViT, custom CNN, Xception integrated with Grad-CAM	HAM10000, ISIC 2018	Accuracy: 96.7%	Lacks multimodal data, over-reliant on visual input	Incorporate patient metadata and textual features for multimodal diagnosis
Gupta, R. K. 2025	Early skin disease prediction with class balancing	CNN + ResNet50 for classification and LIME for local explainability	Custom (Hospital-grade) dataset	Accuracy: 90.1%, Recall: 89.5%	Limited to private dataset, weak generalization	Use public datasets and BOO feature selector for robust generalization
Ieracitano, C. et al. 2025	Quantitative trust score for model	EfficientNet-B0 to assess XAI reliability	ISIC 2020	Accuracy: 92.3%	No spatial consistency for lesion segmentation	Employ SAttNet for precise spatial feature refinement
Kibriya, H. et al. 2025	Explainable melanoma segmentation	Modified UNet with Grad-CAM, resilient to noise/hair artifacts	ISIC 2018	Jaccard: 0.95, Dice: 0.93	No classification or diagnosis output stage	Extend with dual-branch decoder for segmentation + classification
Chanda, T. et al. 2025	Clinical validation using eye-tracking	Human-AI interaction studied via clinician eye movements with XAI	ISIC (subset with annotations)	Accuracy gain: +2.8%	Behavioral insights only; lacks model-side enhancement	Visual attention maps using Grad-CAM & SHAP
Garg, P. et al. 2025	XAI performance across diseases	LIME & Grad-CAM for interpretation	HAM10000	Accuracy: 92.5%	No skin lesion-type specific focus, lacks clinical correlation	Domain-adaptive attention mechanism with lesion-specific refinement
Kumar Saha, D. et al. 2025	Multi-disease ensemble classification	Xception, DenseNet201, EfficientNetB7 + Grad-CAM	MSID	Accuracy: 98.8%	Interpretability limited to Grad-CAM	Design dual-backbone encoder with scalable decoder and SHAP + LIME

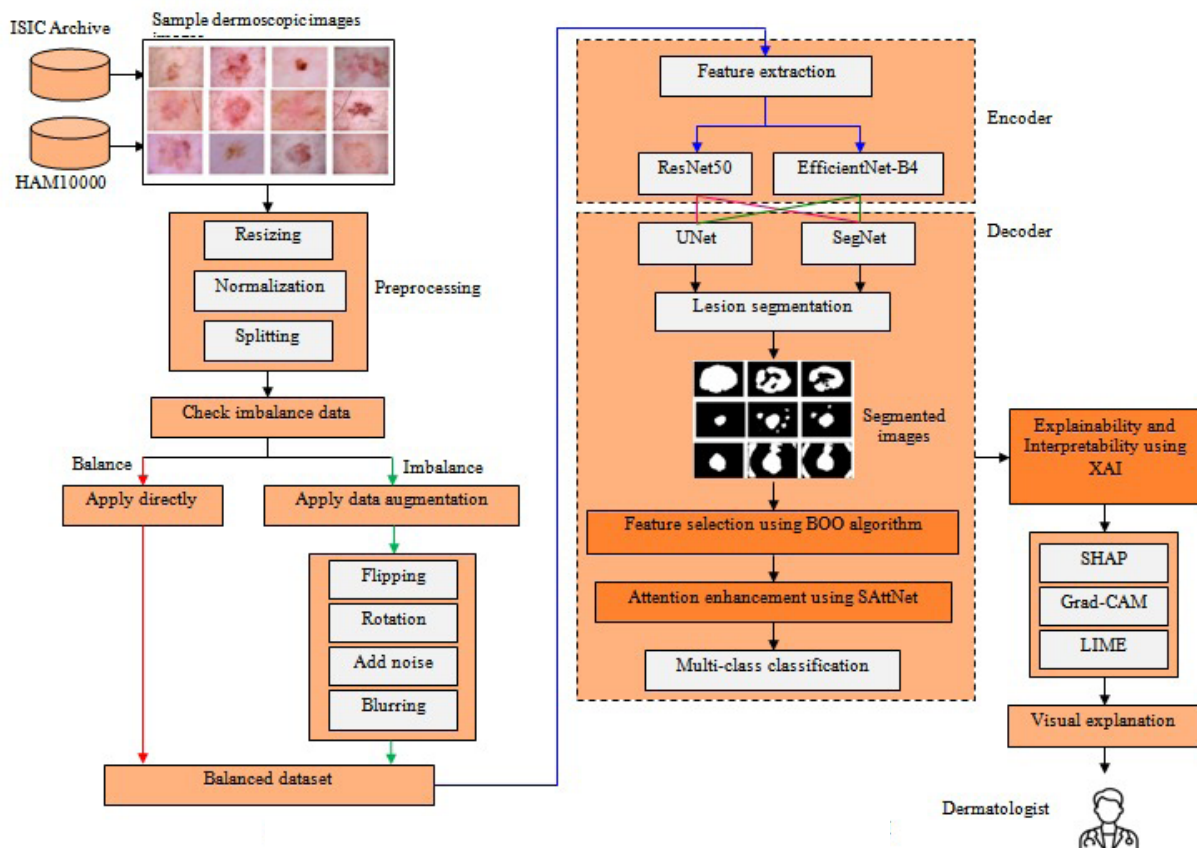


Fig. 1. Skin cancer diagnosis model using optimal encoder and decoder with XAI.

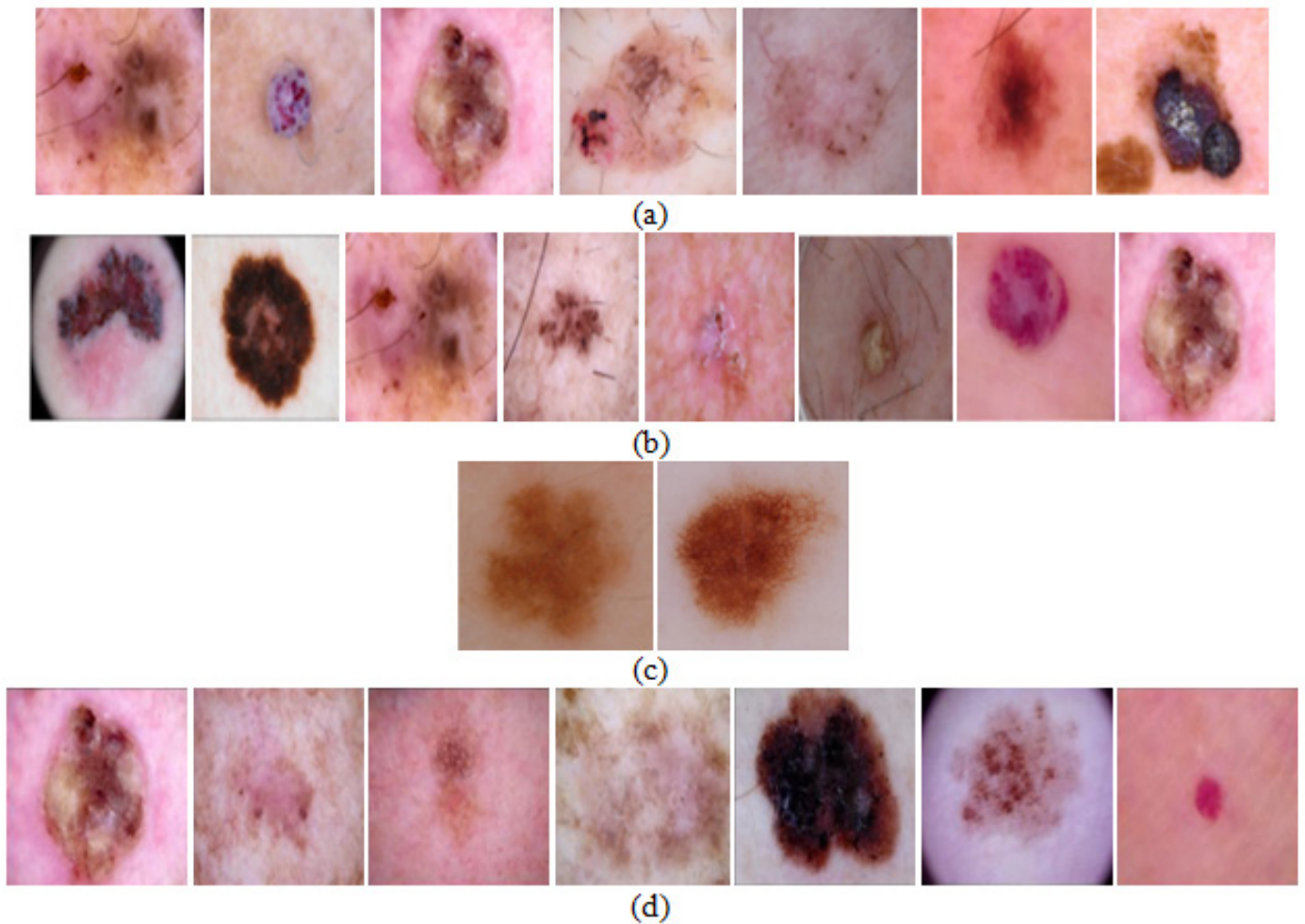


Fig. 2. Sample dermoscopic images of each class from (a) ISIC 2018 [MEL, NV, BCC, AKIEC, BKL, DF, VASC], (b) ISIC 2019 [MEL, NV, BCC, AK, BKL, DF, VASC, SCC], (c) ISIC 2020 [Benign, Malignant], and (d) HAM10000 [AKIEC, BCC, BKL, DF, MEL, NV, VASC].

Table 2. Number of samples before and after data augmentation.

Dataset	Class	Number of samples		
		Original	Augmented	Balanced
ISIC 2018	Melanoma (MEL)	1113	0	1113
	Nevus (NV)	6705	0	6705
	Basal Cell Carcinoma (BCC)	514	486	1000
	Actinic Keratosis (AKIEC)	327	673	1000
	Benign Keratosis (BKL)	1099	0	1099
	Dermatofibroma (DF)	115	885	1000
	Vascular Lesions (VASC)	142	858	1000
ISIC 2019	Melanoma (MEL)	4522	0	4522
	Nevus (NV)	12875	0	12875
	Basal Cell Carcinoma (BCC)	3323	0	3323
	Actinic Keratosis (AK)	867	133	1000
	Benign Keratosis (BKL)	2624	0	2624
	Dermatofibroma (DF)	239	761	1000
	Vascular Lesions (VASC)	253	747	1000
ISIC 2020	Squamous Cell Carcinoma (SCC)	628	372	1000
	Benign	32542	0	32542
	Malignant	584	416	1000

(Contd...)

Dataset	Class	Number of samples		
		Original	Augmented	Balanced
HAM10000	Actinic Keratoses (AKIEC)	327	673	1000
	Basal Cell Carcinoma (BCC)	514	486	1000
	Benign Keratosis (BKL)	1099	0	1099
	Dermatofibroma (DF)	115	885	1000
	Melanoma (MEL)	1113	0	1113
	Melanocytic Nevi (NV)	6705	0	6705
	Vascular Lesions (VASC)	142	858	1000

entire dataset was converted to NumPy arrays, allowing for efficient manipulation, storage, and ingestion by the model. Table 2 shows a summary of the distribution of the samples belonging to different classes in the datasets before and after augmentation.

3.2 Encoder

The encoder, in this case, will be the central element of the automated feature recognition of dermoscopic images. The encoder is also based on the idea of capturing a hierarchy of features (starting with low-level visual features, like edges, contours, and colour gradients, and then high-level semantic features, such as asymmetry, irregular pigmentation, and border discontinuities, which are clinically relevant features of malignancy). In order to obtain strong and various feature representation, the encoder of the proposed framework combines two strong pre-trained convolutional neural network backbones: ResNet50

and EfficientNet-B4. ResNet50 (Firasari, E. et al. 2024) is a 50 layer deep residual network which uses residual learning by using skip connections to successfully overcome the vanishing-gradient problem. EfficientNet-B4 (Dinitra, N. T. et al. 2024) implements a compound-scaling method that is most optimal in terms of network depth, width and input resolution to establish high accuracy and to discriminate between lesion borders, globules, dots, and streak as well as lesions, which are important clinical indicators in skin-cancer.

3.3 Decoder

The decoder plays a vital role in the process of obtaining valid outputs of the encoded feature representations by performing two main functions (i) accurate lesion segmentation and (ii) multi-class skin cancer classification. To achieve the objectives successfully, dedicated decoder architecture is utilized, combining two fully-developed models, including UNet and SegNet models, which, despite being initially defined with a particular focus on biomedical image segmentation, are extended in this case, to serve the purpose of classification. UNet (Kibriya, H. et al. 2025) is an image segmentation network which is designed to use symmetric encoder-decoder architecture, with skip connections to preserve spatial detail. In this context, UNet enables the decoder to retain critical boundary and texture information, which is essential for identifying the irregular shapes and edges of skin lesions. SegNet (Kumar, K. A. and Vanmathi, C. 2024) contributes to structural refinement in the decoding process which enhances semantic segmentation by storing max-pooling indices from the encoder and reusing them during upsampling. SegNet supports the classification branch and helps maintain accurate lesion shapes in the final output.

3.4 Feature selection

The BOO is bio-inspired algorithm used for the skin lesion classification using dermoscopic images (Fig. 3). Drawing inspiration from the bioluminescent behavior of marine organisms such as plankton and jellyfish, which emit light signals for communication, navigation, and survival in the dark ocean depths, BOO mimics these adaptive strategies (Qin, X. et al. 2024) to navigate the complex, high-dimensional feature space derived from dermoscopic image data. The mechanism of attraction and repulsion describes how the agents tend to gravitate towards more informative sets of features -through brighter agents, and also avoids suboptimal sets of features, and thus equilibrium between

exploration and exploitation is maintained (Halbers, L. P. et al. 2024). Unlike other traditional paradigms like the GA, PSO, and ACO (Wu, Y. et al. 2025), which often undergo premature convergence and early exploration, BOO uses light based signaling to guide agents to optimal informative feature subsets. The agents (M) are represented either by a binary vector (mY) or by a real-valued one (mY, P) representing the selection status of the features (mY C), and the initialization of the whole population of BOO is performed in the following way.

$$M = \begin{bmatrix} M_1 \\ \vdots \\ M_h \\ \vdots \\ m_Y \end{bmatrix}_{Y \times c} = \begin{bmatrix} m_{1,1} & \cdots & m_{1,g} & \cdots & m_{1,c} \\ \vdots & \ddots & \vdots & \ddots & \vdots \\ m_{h,1} & \cdots & m_{h,g} & \cdots & m_{h,c} \\ \vdots & \ddots & \vdots & \ddots & \vdots \\ m_{Y,1} & \cdots & m_{Y,g} & \cdots & m_{Y,p} \end{bmatrix}_{Y \times c} \quad (1)$$

The initial state of the bioluminescent agents in the search space is generated using randomized initialization at the beginning of the algorithm execution, where each agent represents a candidate feature subset for the classification task.

$$m_{h,g} = Ly_g + R_{h,g} \cdot (Uy_g - Ly_g), \quad h = 1, 2, \dots, Y, \quad \text{and} \quad g = 1, 2, \dots, c, \quad (2)$$

Here, M represents the population matrix of bioluminescent agents, where the h-th agent (a candidate feature subset) and its g-th dimension correspond to a specific decision variable (feature) in the search space. Y denotes the whole numeral of agents, and d is the numeral of features (decision variables). The values are initialized using random numbers in the interval [0, 1]. Each agent thus represents potential feature combination and evaluates the objective function based on its selected feature set.

$$F = \begin{bmatrix} f_1 \\ \vdots \\ f_h \\ \vdots \\ f_Y \end{bmatrix}_{Y \times 1} = \begin{bmatrix} f(M_1) \\ \vdots \\ f(M_h) \\ \vdots \\ f(M_Y) \end{bmatrix}_{Y \times 1} \quad (3)$$

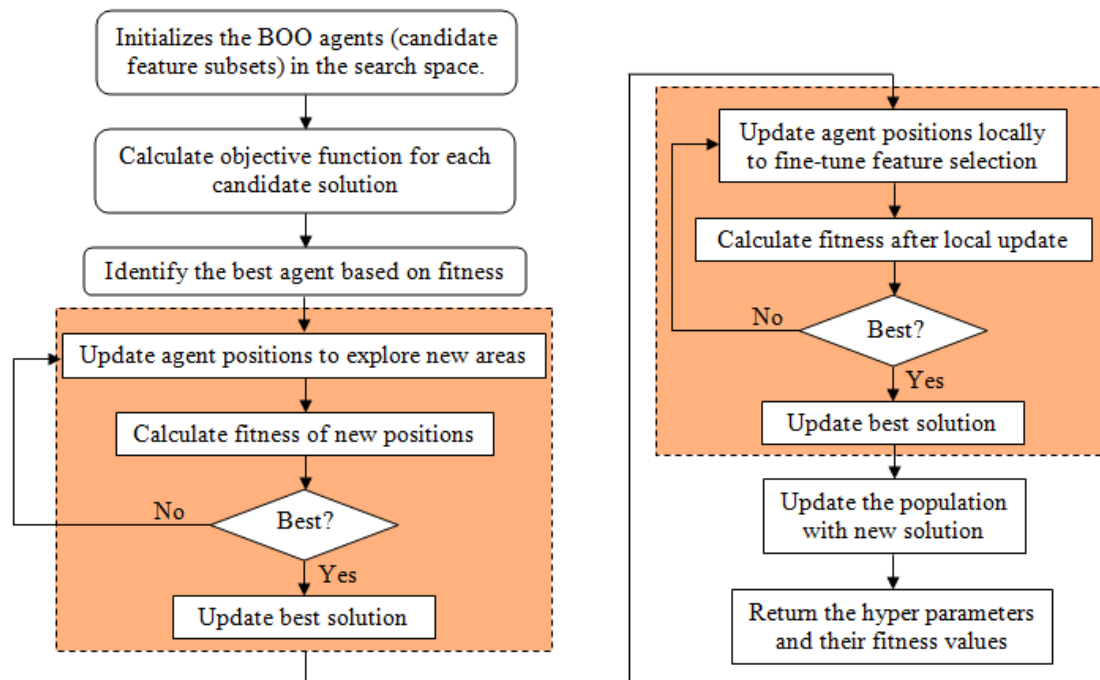


Fig. 3. BOO algorithm for feature selection.

The vector F represents the objective function values corresponding to each candidate feature subset in the population. The global search strategy enhances diversity and helps avoid premature convergence.

$$m_{h,g}^{X1} = p_{h,g} + R_{h,g} \cdot (A_g - H_{h,g} \cdot p_{h,g}), \quad h = 1, 2, \dots, Y, \quad \text{and} \quad (4)$$

$$g = 1, 2, \dots, c,$$

This represents a scenario where a bioluminescent agent explores a promising region in the search space by moving toward the best-known feature subset (i.e., the current optimal solution).

$$M_h = \begin{cases} M_h^{A1}, & f_h^{A1} < f_h \\ M_h, & \text{else,} \end{cases} \quad (5)$$

where M_h^{A1} represents the new location of the h -th founded on the first phase, $m_{h,g}^{X1}$ is its g -th dimension, f_h^{A1} is its objective function worth, $R_{h,g}$ are random statistics in interval $[0, 1]$.

$$m_{h,g}^{A2} = m_{h,g} + \frac{R_{h,g} \cdot (Un_g - Ln_g)}{s}, \quad h = 1, 2, \dots, B, \quad g = 1, 2, \dots, c, \quad \text{and} \quad (6)$$

$$s = 1, 2, \dots, S$$

If the newly generated feature subset improves the objective function—such as classification accuracy or feature compactness—it replaces the previous subset for that agent, ensuring continuous enhancement of the solution quality.

$$M_h = \begin{cases} M_h^{A2}, & f_h^{A2} < f_h \\ M_h, & \text{else,} \end{cases} \quad (7)$$

Based on the M_h^{A2} second phase of BOO algorithm, h -th represents the new state of the fitness, $m_{h,g}^{A2}$ its g -th measure f_h^{A2} represents its objective function. Upon completion, the best feature subset identified throughout the optimization process is selected as the final optimal solution for feature selection.

3.5 Attention enhancement

Attention enhancement refers to the use of mechanisms that assist the typical to emphasis selectively on the most important areas of the dermoscopic imageries, particularly the areas around lesion boundaries

that are critical for accurate diagnosis. The SAttNet is used to refine the article maps generate by the strength system by emphasizing diagnostically relevant information while suppressing irrelevant background noise. SAttNet (Ocal, H. 2024) works by first performing a squeeze operation, such as comprehensive regular pooling, to aggregate spatial info into a compact descriptor. As shown in Fig. 4, SAttNet captures rich multi-scale longitudinal structures and efficiently begin long-term $F_p \in R^{D \times I \times Z}$ relationships between channel foci at different scales. D stands for the numeral of networks in an input article map, whereas I and Z stand for the feature map's size. To improve the volume's depiction of vascular characteristics, the feature maps of every branch were included.

Based on the bifurcated input paradigm F_t^Y , the computation that can be performed on each branch of the transition (T_{eff}) is as the following:

$$F_t^Y = T_{eff} \left(Z_{p_y}, Kr^{z_y}, L^{z_a} \right) \quad y = 1, 2, \dots, Y \quad (8)$$

The non-linear vector quantization f_{conv} belongs to the attention mechanism with the objective function $K^{(a)}$ and the kernel size is fixed by convolutional vector. The fitness optimization f_{conv} performs by the maximum threshold vector follows the optimal solution allows to reach convergence matrix ($J^{(a)}$). The joint cluster vector allows fixing the convolutional layer in the Attention mechanism.

$$t^{(a)} = f_{se}(F_t^{(y)}) \quad (9)$$

The weight part consists of two stages; compression and excitation. The feature map's J_{dis} spatial dimension is compressed using the average aggregation. The objective function of each candidates follows the maximum rule-set theory to fix the optimal solution.

$$J_{dis} = \max \frac{1}{TH(Z^Y)} \int \sum_{y=1}^{Y1} (f_{ex} + F_d(h, g)) \quad (10)$$

Two repeated fully linked deposits were utilized to learn and give masses to every frequency during the stimulus phase, reflecting the significance belongs to distance between threshold vectors (T_{diff}).

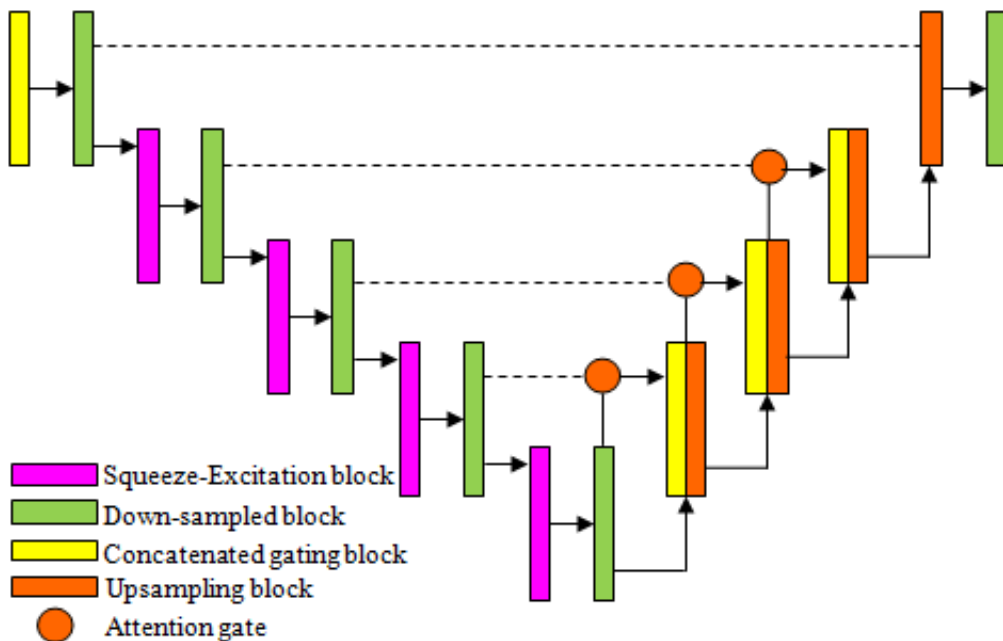


Fig. 4. Construction of SAttNet.

$$T_{diff} = \partial_{ex} \left(\sum_{y=1}^{Y1} J_{dis}, t^a, J_{dis} \right) \quad (11)$$

The optimal vector function is used to formulate the maximum threshold J_d function by using the ReLU. The control vector for convolutional layer is formulated by the sigmoid function $Att^{(a)}$ with the difference between minimum Z_1 and maximum Z_2 threshold vectors.

$$Att^{(a)} = f_{soft\ max}(t^{(a)}) = Exp \frac{T_{diff}}{\sum_{a=1}^A Exp(t^{(a)})} \quad (12)$$

The channel consideration is considered a viable aspect in the segmented function $F_t^{(a)}$, which allows the linear vector formation to the attention module.

$$F_{out}^{(a)} = Att^{(a)} \odot F_t^{(a)} \quad (13)$$

The control values for fixed attention vector are compute through the maximum threshold.

The collections of oral records, catalogued in terms of frequency, are thrown away to come up with the final cartographic image as demonstrated by the resulting tracks:

$$F_{out} = concat([F_{out}^{(1)}, F_{out}^{(2)}, \dots, F_{out}^{(A)}]) \quad (14)$$

In this context, the Multi-Scale Attention (MSA) component $F_{out} \in R^{D \times I \times Z}$ is generated by a multiplicity of calibrated processes. The loss utility l_{Dice} and l_{cldice} can be expressed as the weighted aggregation of the relevant metrics and loss functions, as explicated in the further analyses.

$$L = (1 - \alpha)l_{Dice} + \alpha l_{cldice} \quad (15)$$

The vessel subdivision l_{Dice} is accurate or not depends on a confluence of disciplinary views l_{cldice} which affect, in their turn, the richness of l_{Dice} the receptacle structure which lies behind them. In this regard, the predetermined mindset about a balance problem that occurs due to the presence of various influencing factors is an issue l_{cldice} . The rational feature separation predictive model and v_g correspondence through the Dice loss function are customized as the following.

$$L_{dice} = 1 - \frac{2 \times |v_x \cap v_g| + smooth}{|v_x| + |v_g| + smooth} \quad (16)$$

The smooth quantization vector (L_{SQV}) is optimal function to fix the threshold by the occurrence mutual vectors.

$$L_{SQV} = v_x \nabla v_g \frac{L_{smooth} \cup L_{max} \cap L_{dice}}{L \wedge F_{out} \vee T_{diff}} \quad (17)$$

The random solution follows the square low to fix the quality measure functions of decision model which fix the objective function of linear topological vector.

3.6 Explainability and interpretability

An XAI is incorporated to help alleviate this problem by allowing the model's predictions to be interpreted both locally and globally.

- The gradient-weighted class activation mapping (Grad-CAM) (Na, A. 2024) is used to generate visual explanations by produces heatmap over input images. The geographical areas that the model concentrates on while generating categorization decisions are highlighted in these Heatmaps.
- The SHAP (Hu, B. et al. 2024) offers a quantitative interpretation by assigning each feature a contribution value based on influence on the model's output. SHAP provide both global insights and local insights, making it highly valuable for model debugging and validation.
- The local interpretable model-agnostic explanation (LIME) (Mahmud, M. Z. et al. 2024) complements these methods by offering instance-specific explanations. For each input case—such as a patient's dermoscopic image—LIME identifies and visualizes which specific regions most influenced the model's classification.

4. Results Analysis

The consequences of the investigation of the skin cancer diagnostic models using benchmark datasets are described in this section. TensorFlow and PyTorch libraries were used in Python 3.11 to implement and run all of the experiments that were discussed. The experiments were performed using a Windows operating system, and the processor was an Intel Core i7-10th generation with 8GB RAM. An Nvidia RTX 2060 graphics processing unit with 6 GB of dedicated memory was used to speed up the training and computational processes. The dataset was initially disconnected into predefined exercise and difficult sets. During runtime, the training data was split using K-fold cross-validation, maintaining a consistent 70:30 ratio between exercise and authentication subsets.

4.1 Impact of feature selection in skin cancer diagnosis

The experimental analysis presented in Fig. 5 for the ISIC Archive dataset evaluates the performance of six feature selection algorithms—GA, PSO, GWO, WOA, ACO, and BOO—across three key metrics:

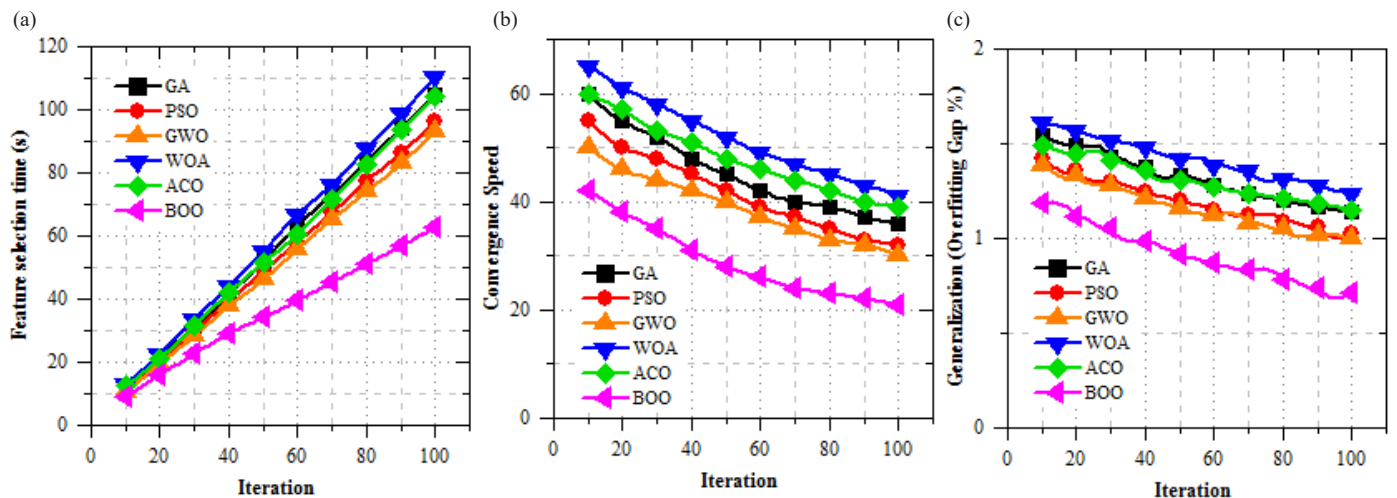


Fig. 5. Results of feature selection algorithms for ISIC Archive dataset (a) Feature selection time, (b) Convergence Speed, (c) Generalization (Overfitting Gap %).

Table 3. Computational complexity comparison of feature selection algorithms.

Algorithm	Average computation time (s)	Iteration count	Theoretical complexity	Relative complexity level
GA	118.421	100	$O(N \times D \times G)$	High
PSO	103.572	100	$O(N \times D)$	Moderate-High
GWO	91.334	80	$O(N \times D)$	Moderate
WOA	87.255	80	$O(N \times D)$	Moderate
ACO	126.485	120	$O(N^2 \times D)$	High
BOO	64.198	60	$O(N \times D)$	Low

feature selection time, convergence speed, and generalization. BOO is also shown to be significantly better than other algorithms in all the metrics evaluated in both figures. These comparative findings provide conclusive evidence that burrow-based owl optimization (BOOW) is the most efficient feature-selection tool in the set of tools considered, with the shortest processing time, the fastest convergence, and the best generalization performance, which makes it appropriate for the target of detecting skin-lesions in dermatological data. The findings indicate that EfficientNet-B4+UNet+BOO+SAttNet model has the best performance in the skin cancer diagnosis, offering high classification accuracy, strong generalization, and decent class-level discrimination in all lesion types in the ISIC 2018 dataset. The efficiency of the proposed BOO algorithm can be clearly seen in the comparative analysis of the computational complexity of various feature-selection algorithms, which is available in Table 3. BOO has the shortest average time of computation, that is equal to 64.19s with just 60 iterations, indicating a 45.81% reduction with respect to GA, 38.01% reduction with respect to particle swarm optimization (PSO), 29.7% reduction with respect to GWO, 26.4% reduction with respect to whale optimization algorithm (WOA), and 49.25% reduction with respect to ant colony optimization (ACO). It is an improvement that highlights the better optimization and convergence, and capabilities of BOO. Its computational efficiency is also supported by the fact that the corresponding theoretical complexity of the $O(N \times D)$ is lower than its competitors, including GA and ACO,

have higher complexities of $O(N \times D \times G)$ and $O(N^2 \times D)$ respectively, which in turn increases their run time. The success of light-intensity-based exploration mechanism enabling adaptability of BOO has largely contributed to its success in gaining performance in terms of exploitation and exploration, reducing unnecessary evaluations, and convergence speed.

4.2 Performance analysis of ISIC 2018 dataset

The experimental outcomes shown in Fig. 6 give a detailed comparison between a number of advanced model of learning under four important performance measures; Accuracy, Precision, Recall, and F-measure- within the framework of skin lesion classification. The architecture that included EfficientNet-B4, UNet, BOO, and SAttNet provided the best accuracy results of all lesion types, where the result was as high as 99.817% on nevus (NV), 99.786% on benign keratinocyte lesions (BKL), and consistently high results on the other classes (MEL, NV, BCC, AKIEC, BKL, DF, VASC). The setup that used EfficientNet-B4, SegNet, BOO, and SAttNet yielded slightly worse but still very competitive results, which demonstrates that both UNet and SegNet frameworks can be effectively used with the help of BOO and SAttNet modules. On precision, once again EfficientNetB4UNetBOO SAttNet setup performed better with top scores in NV of 99.803% and BKL of 99.761% with low false positives. The same pattern was observed in the case of recall values as the same model obtained 99.791% for NV, 99.737% in basal cell carcinoma (BCC), and the lowest inter-class deviation. The F- measure that weighs precision and recall was also the highest at this composition in all classes reaching 99.796% in the case of NV and 99.752% in the case of BKL hence indicating an optimal trade-off in classification. From Figs. 7 and 8 shows that the BOO optimization algorithm significantly improved performance across all metrics. When comparing models with and without BOO, the performance uplift is clearly visible. For example, ResNet50+UNet+SAttNet had a maximum accuracy of 99.187%, while with BOO, the improved version (ResNet50+UNet+BOO+SAttNet) achieved up to 99.583%.

4.3 Performance analysis of the ISIC 2019 dataset

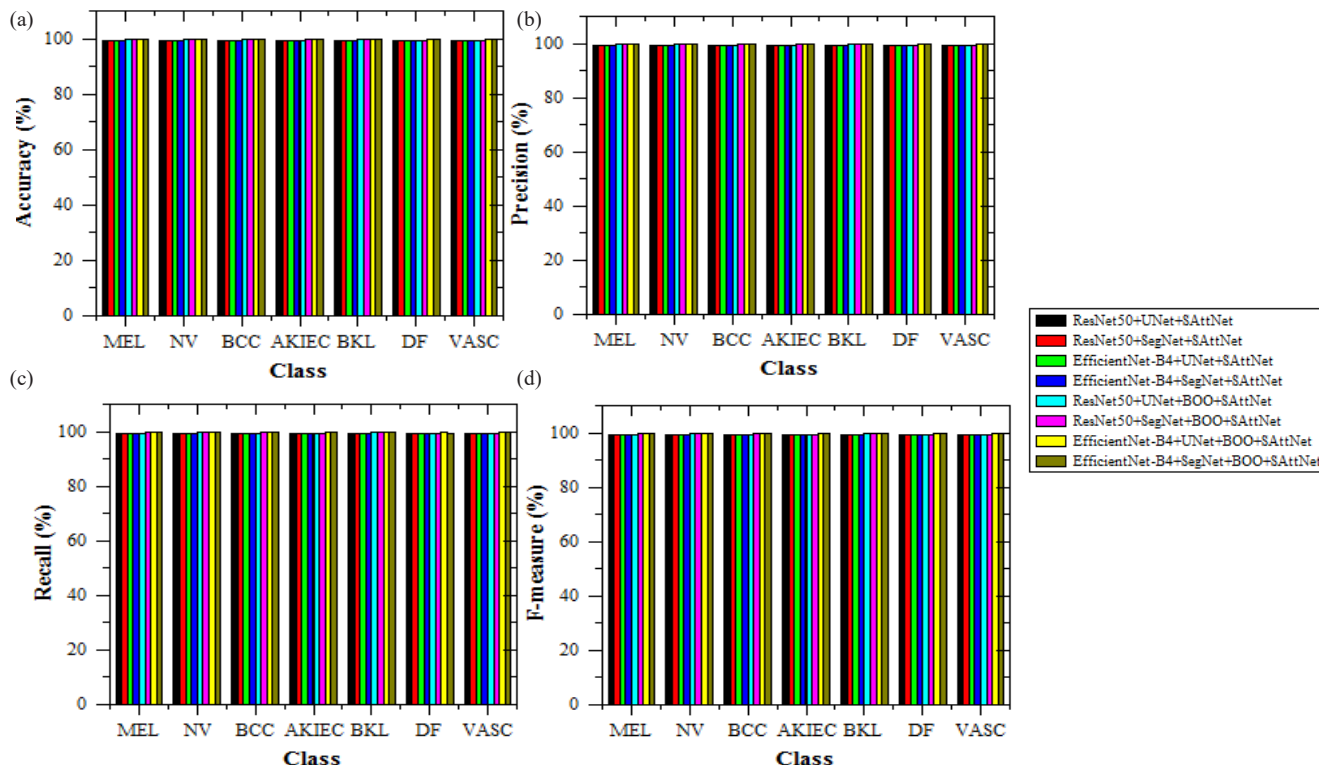


Fig. 6. Results of proposed models for ISIC 2018 dataset (a) Accuracy, (b) Precision, (c) Recall, and (d) F-measure.

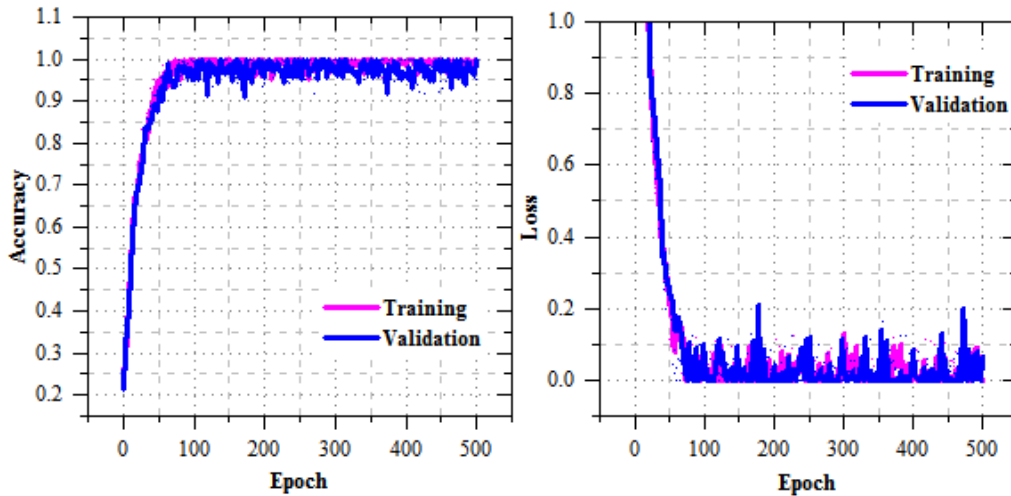


Fig. 7. Training and Validation performance of the proposed model for skin cancer diagnosis on the ISIC 2018 dataset (a) Accuracy (b) Loss.

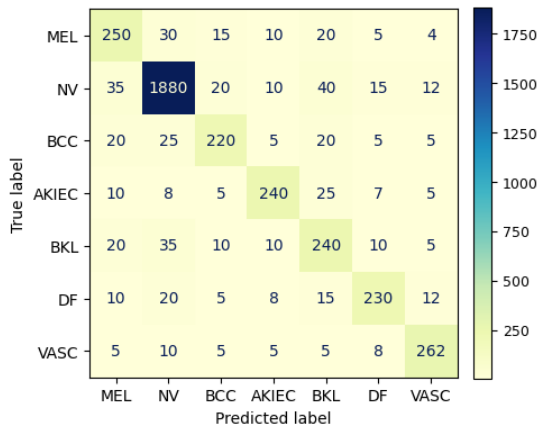


Fig. 8. Confusion matrix for ISIC 2018 dataset.

The quantitative analysis shown in Fig. 9 evaluates the presentation of several deep learning configurations over eight skin lesion classes—MEL, NV, BCC, AK, BKL, DF, VASC, and SCC—using the ISIC 2019 dataset. The most successful classification accuracy was observed with the EfficientNet-B4+UNet+BOO+SAttNet architecture, with the performance metrics ranging between 99.589% seborrheic keratosis (SCC) to 99.816% nevi (NV), and thus proving to have a strong discriminative performance across regularly and uncommonly observed lesion subtypes. Fig 9-11 of the experimental analyses show that the EfficientNet-B4+UNet+BOO+SAttNet model is offering the best and consistent results in all the eight types of lesions in the ISIC 2019 dataset. Both the integration of the BOO strategy can help optimize and converge more efficiently. The SAttNet module can complement spatial feature awareness and make the suggested architecture especially suitable to be implemented as a practical clinical decision-support device in skin-cancer diagnostics.

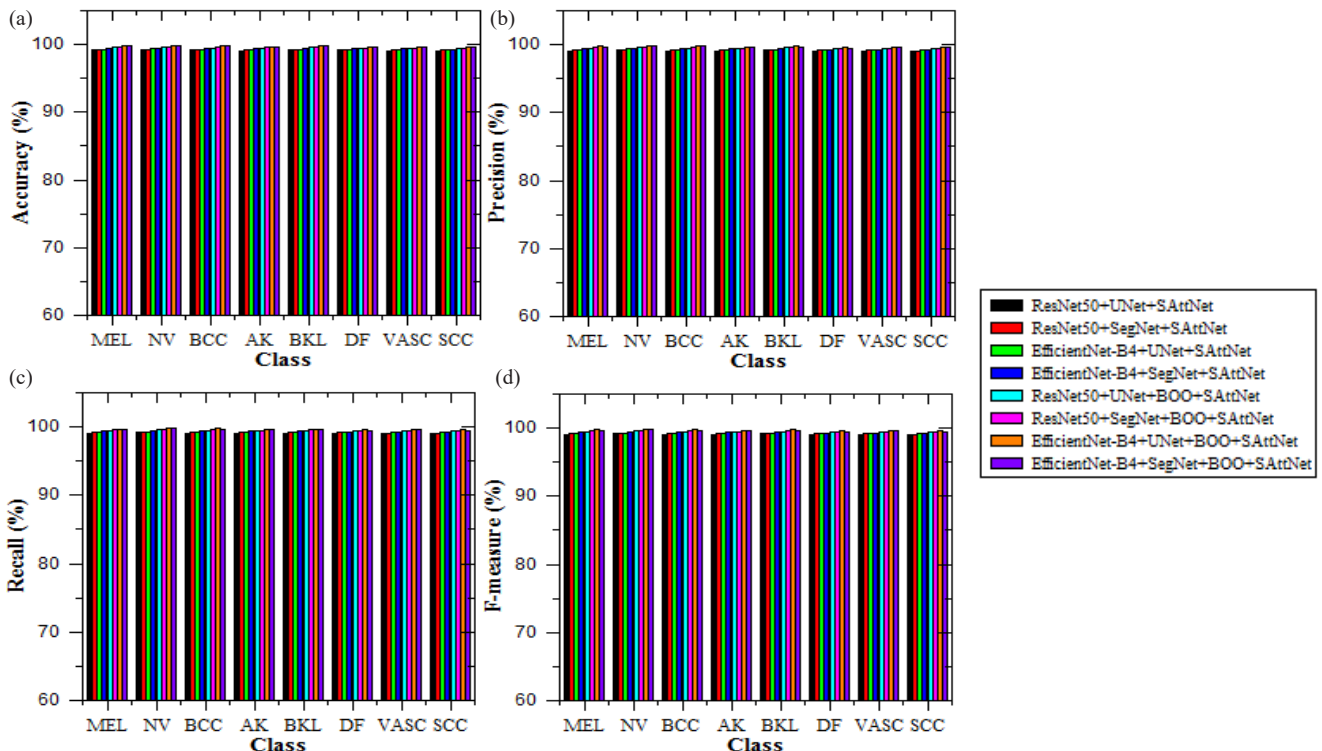


Fig. 9. Results of proposed models for ISIC 2019 dataset (a) Accuracy, (b) Precision, (c) Recall, and (d) F-measure.

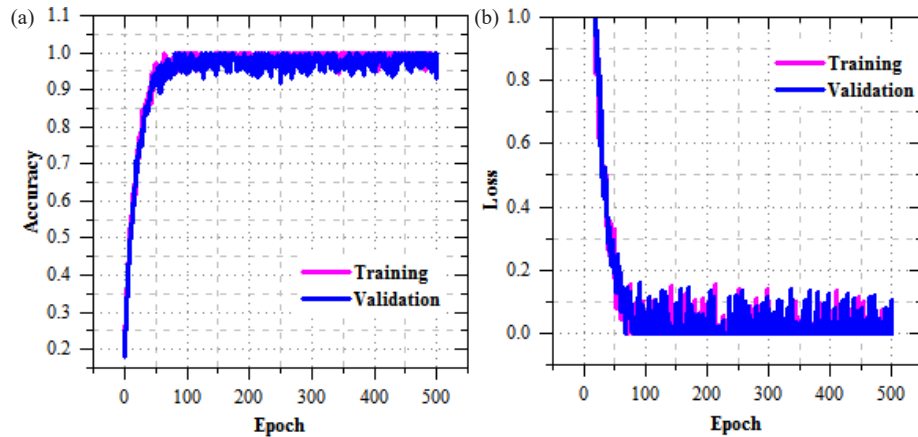


Fig. 10. Training and Validation performance of the proposed model for skin cancer diagnosis on the ISIC 2019 dataset (a) Accuracy (b) Loss.

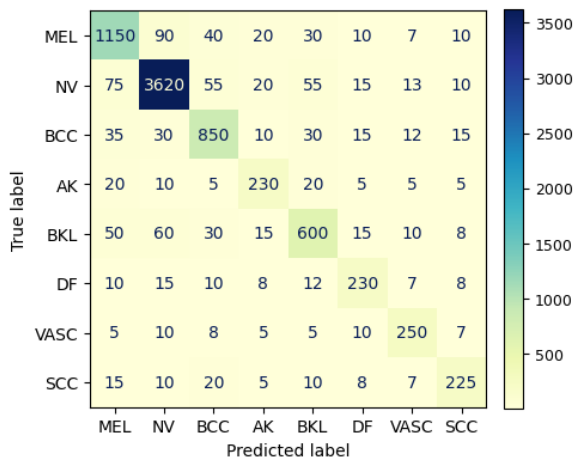


Fig. 11. Confusion matrix for ISIC 2019 dataset.

4.4 Performance analysis of the ISIC 2020 dataset

The results of the comparison of the performance of a few hybrid deep-learning models on the ISIC 2020 data on skin-cancer classification are shown in Fig. 12. The EfficientNet-B4+UNet+BOO+SAttNet setup was the most successful in its comparison, and had the highest rates of accuracy of 99.742% on the Benign and Malignant classes, respectively. The combination of the BOO and SAttNet was important in the refined feature selection and spatial attention respectively, led to an increased confidence in lesion recognition and classification respectively. As it can be seen in Figs. 12-14, the EfficientNet-B4+UNet+BOO+SAttNet model provides high and stable results on all the eight lesion types in the ISIC 2020 dataset. The BOO component helps to improve optimization and convergence, and the SAttNet module is used to improve the awareness of the spatial features, but the given architecture is extremely appropriate to the practical clinical decision-support in skin-cancer diagnostics.

4.5 Performance analysis of HAM10000 dataset

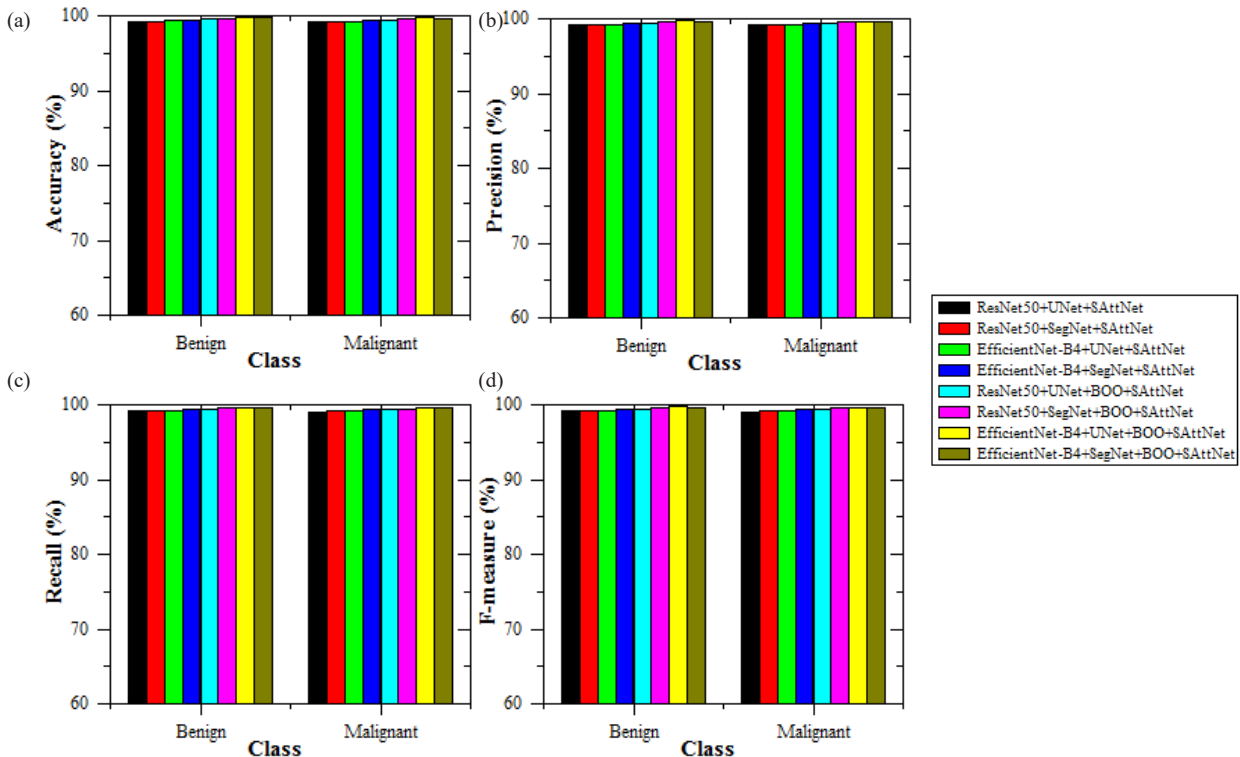


Fig. 12. Results of proposed models for ISIC 2020 dataset (a) Accuracy, (b) Precision, (c) Recall, and (d) F-measure.

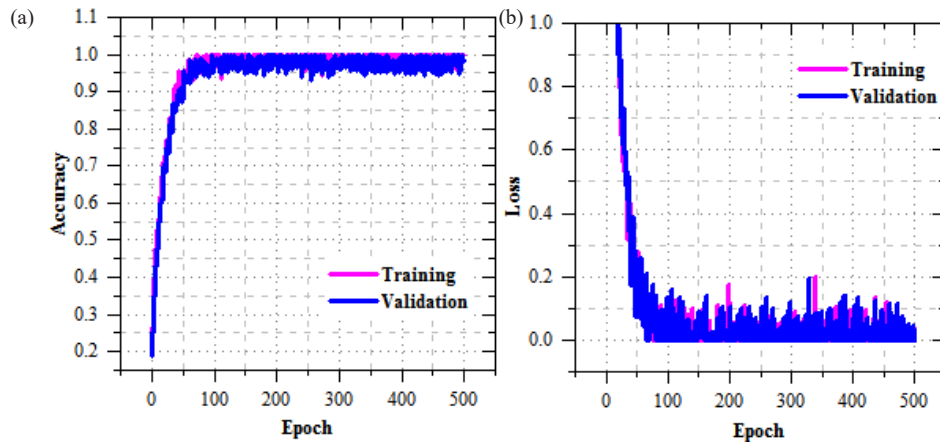


Fig. 13. Training and Validation performance of the proposed model for skin cancer diagnosis on the ISIC 2020 dataset (a) Accuracy (b) Loss.

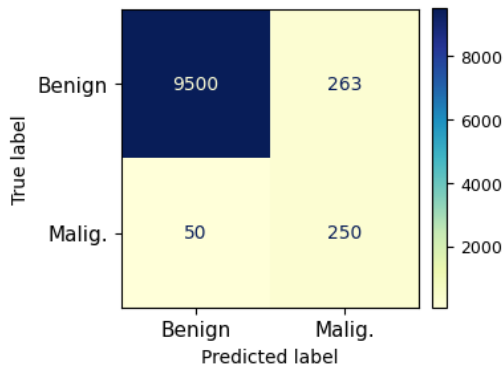


Fig. 14. Confusion matrix for ISIC 2020 dataset.

As shown in Fig. 15, the experimental assessment of HAM10000 dataset is a detailed, class-related analysis of the suggested models in the seven skin-lesion categories actinic keratoses and intraepithelial carcinoma (AKIEC), Basal cell carcinoma (BCC), Benign keratosis-like lesions (BKL), Dermatofibroma (DF), Melanoma (MEL), Melanocytic nevi (NV), and Vascular lesions efficientNet-B4 – Efficient network (Baseline-4 variant)+U-shaped network (UNet)+Bioluminescent ocean optimization (BOO)+Squeeze attention network (SAttNet) model supported by AKIEC, NV, and VASC resulted in an accuracy of 99.687%, 99.831%, and 99.707% which indicated its ability to classify both uncommon and common type of lesions with an exceptionally high degree of accuracy. On precision, BCC and NV had a 99.742% and 99.799%, respectively, which is excellent; it represents an excellent proportion of truly identifying a positive result with a low number of false positives. The strong sensitivity of the model in identifying even the most visually ambiguous classes was supported by the recall values

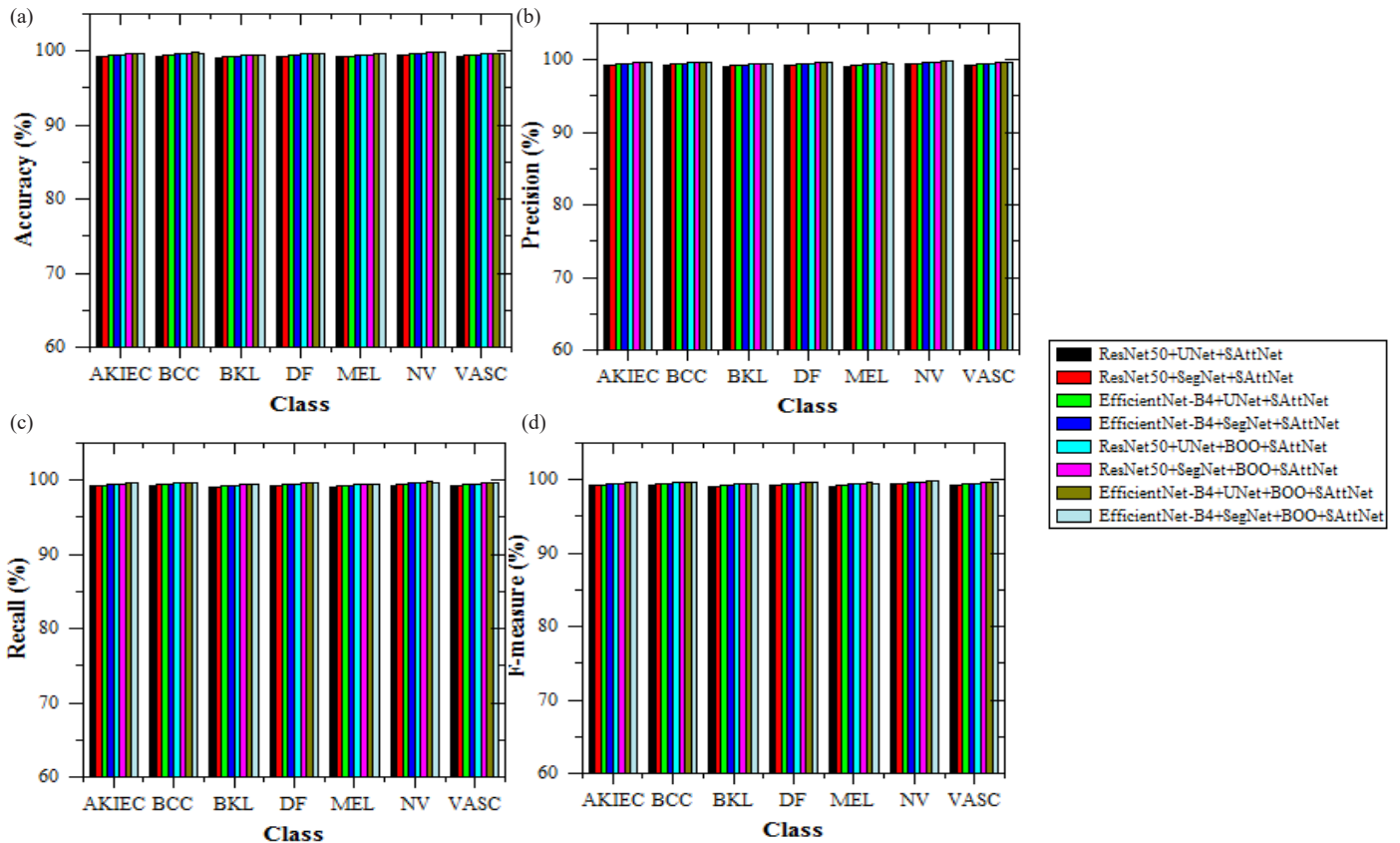


Fig. 15. Class-wise result analysis of proposed models for HAM10000 dataset (a) Accuracy, (b) Precision, (c) Recall, and (d) F-measure.

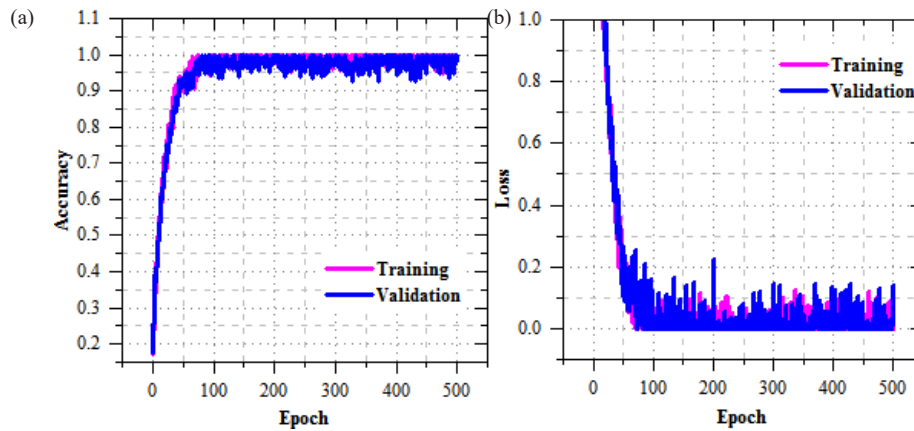


Fig. 16. Training and Validation performance of proposed model for skin cancer diagnosis on HAM10000 dataset (a) Accuracy (b) Loss.

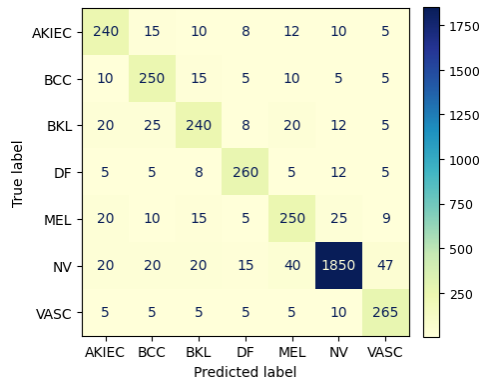


Fig. 17. Confusion matrix for HAM10000 dataset.

of 99.547% of MEL and 99.724% of BCC. The F-measure scores of 99.733% BCC and 99.783% NV supported the consistency and validity of the model in the accuracy and consistency in complex cases with overlapping features. Figs. 15-17 also indicate that EfficientNet-B4+UNet+BOO+SAttNet model gives better and stable results in all the eight lesion classes of HAM10000 dataset. BOO addition improves optimization and convergence, and the SAttNet addition improves spatial feature knowledge, which is why the proposed model is extremely applicable in real-life clinical decision-support in skin-cancer diagnosis.

5. Discussion

The suggested model, EfficientNet-B4+SegNet+BOO+SAttNet, is related in contradiction of the state-of-the-art models using the ISIC

Table 4.

Results comparison of proposed and existing state-of-the-art models for skin cancer diagnosis across different datasets.

Dataset	Models	Values in %		
		Accuracy	Sensitivity	Specificity
ISIC 2018	Extreme learning machine (ELM) (Purni, J. T. and Vedhapriyavadhana, R. 2024)	82.500	–	–
	Logistic regression (LR) (Purni, J. T. and Vedhapriyavadhana, R. 2024)	86.250	–	–
	Multilayer perceptron (MLP) (Purni, J. T. and Vedhapriyavadhana, R. 2024)	88.750	–	–
	Convolutional neural network (CNN) (Purni, J. T. and Vedhapriyavadhana, R. 2024)	89.440	–	–
	CNN-EOSA (Purni, J. T. and Vedhapriyavadhana, R. 2024)	93.050	–	–
	Xception (Shah, S. A. H. et al. 2024)	89.700	93.900	84.600
	Xception+Gaussian SVM (Shah, S. A. H. et al. 2024)	89.600	93.400	85.500
	Xception+PSO+KNN (Shah, S. A. H. et al. 2024)	98.500	98.100	98.900
	EfficientNet-B4+SegNet+BOO+SAttNet	99.688	99.653	99.389
ISIC 2019	Extreme learning machine (ELM) (Purni, J. T. and Vedhapriyavadhana, R. 2024)	84.270	–	–
	Logistic regression (LR) (Purni, J. T. and Vedhapriyavadhana, R. 2024)	88.670	–	–
	Multilayer perceptron (MLP) (Purni, J. T. and Vedhapriyavadhana, R. 2024)	90.550	–	–
	Convolutional neural network (CNN) (Purni, J. T. and Vedhapriyavadhana, R. 2024)	92.780	–	–
	CNN-EOSA (Purni, J. T. and Vedhapriyavadhana, R. 2024)	97.870	–	–
	DenseNet201 (Al-Rasheed, A. et al. 2022)	92.000	90.000	93.000
	SCSO-ResNet50-EHSCNN (Akilandasowmya, G. et al. 2024)	92.000	93.900	85.500
	ViT+MobileNet (Altman, N. S. 1992)	91.200	93.000	90.000
	EfficientNet-B4+SegNet+BOO+SAttNet	99.673	99.625	99.412
HAM10000	CGAN+Ensembled (Raju, K. K. et al. 2023)	86.000	84.000	88.000
	Custom CNN (Ali, M. S. et al. 2021)	93.000	91.000	94.000
	ViT+CNN (Ahmad, I. et al. 2024)	90.000	92.000	89.000
	Xception+PSO+KNN (Purni, J. T. and Vedhapriyavadhana, R. 2024)	86.100	91.420	64.310
	EfficientNet-B4+SegNet+BOO+SAttNet	99.656	99.594	99.568

Table 5. Results comparison of proposed model with existing models in literature review for skin cancer diagnosis across different datasets.

Dataset	Model	Accuracy (%)
HAM10000	Meta-XPFL with XAI (Purni, J. T. and Vedhapriyavadhana, R. 2024)	94.200
ISIC 2019	IARS SegNet (Firasari, E. et al. 2024)	95.632
ISIC Archive	YOLOv8+ViT+SHAP&Grad-CAM (Dinitra, N. T. et al. 2024)	93.000
HAM10000	ViT+CustomCNN+Xception+Grad-CAM (Kibriya, H. et al. 2025)	96.700
Custom	CNN+ResNet50+LIME (Kumar, K. A. and Vanmathi, C. 2024)	90.100
ISIC 2020	EfficientNet-B0 (Qin, X. et al. 2024)	92.300
ISIC 2018	Modified UNet+Grad-CAM (Halbers, L. P. et al. 2024)	87.562
ISIC Archive	Grad-CAM+SHAP (Wu, Y. et al. 2025)	96.325
HAM10000	LIME+Grad-CAM (Ocal, H. 2024)	92.500
MSID	EfficientNetB7+Grad-CAM (Na, A. 2024)	98.800
ISIC 2018	EfficientNet-B4+SegNet+BOO+SAttNet	99.688
ISIC 2019	EfficientNet-B4+SegNet+BOO+SAttNet	99.673
ISIC 2020	EfficientNet-B4+SegNet+BOO+SAttNet	99.685
HAM10000	EfficientNet-B4+SegNet+BOO+SAttNet	99.656

2018, ISIC 2019, and HAM10000 datasets in Table 4. The model obtained 99.688% accuracy, 99.653% sensitivity, and 99.389% specificity on the ISIC 2018 dataset. Compared to the best-performing existing model, Xception+PSO+KNN (Shah, S. A. H. et al. 2024), this represents a 1.20% increase in accuracy, 1.58% gain in sensitivity, and 0.49% improvement in specificity. In comparison with CNN-EOSA (Purni, J. T. and Vedhapriyavadhana, R. 2024), the accuracy improved by 7.11%. For the ISIC 2019 dataset, the wished-for model attained an accuracy of 99.673%, sensitivity of 99.625%, and specificity of 99.412%. These results show .84% increase in accuracy over CNN-EOSA (Purni, J. T. and Vedhapriyavadhana, R. 2024), and against DenseNet201 (Al-Rasheed, A. et al. 2022), an improvement of 8.33% in accuracy, 9.58% in sensitivity, and 6.91% in specificity. Compared to SCCSO-ResNet50-EHSCNN (Akilandasowmya, G. et al. 2024), the proposed model shows gains of 8.34% in accuracy, 5.72% in sensitivity, and 13.93% in specificity. On the HAM10000 dataset, the anticipated model accomplished an exactness of 99.656%, sensitivity of 99.594%, and specificity of 99.568%. When compared with Custom CNN (Ali, M. S. et al. 2021), this shows an improvement of 7.15% in accuracy, 9.45% in sensitivity, and 5.96% in specificity. Against ViT+CNN (Ahmad, I. et al. 2024), the improvement is 0.73% in accuracy, 8.70% in sensitivity, and 11.86% in specificity. Compared to Xception+PSO+KNN (Purni, J. T. and Vedhapriyavadhana, R. 2024), the accuracy increased by 13.68%, sensitivity by 8.17%, and specificity by an exceptional 35.26%. The findings unequivocally show that the model performs better than earlier approaches on all datasets and assessment measures, indicating a high probable for applied clinical uses in the detection of skin cancer. Table 5 presents a comparison of the proposed EfficientNet-B4+SegNet+BOO+SAttNet model with existing models from the literature across various datasets for skin cancer diagnosis. On the ISIC 2018 dataset, the proposed model achieved an accuracy of 99.688%, which shows a 12.12% improvement over the Modified UNet+Grad-CAM (Kibriya, H. et al. 2025), which is 87.562% accuracy. Compared to Grad-CAM+SHAP (Chanda, T. et al. 2025), which attain 96.325%, the proposed model improved by 3.49%. For the ISIC 2019 dataset, the proposed model achieved 99.673% accuracy, which outperformed the IARS SegNet (Narayanan, V. S. et al. 2024) model (95.632%) by 4.22%. This also marks a 6.67% gain over the complex YOLOv8+ViT+SHAP&Grad-CAM model (AbuAlkebash, H. et al. 2025) which achieved only 93.0%. On the ISIC 2020 dataset, the proposed model achieved 99.685%, 7.99% improvement over the EfficientNet-B0 model (Qin, X. et al. 2024), which scored 92.3%. For HAM10000 dataset, the proposed model recorded an accuracy

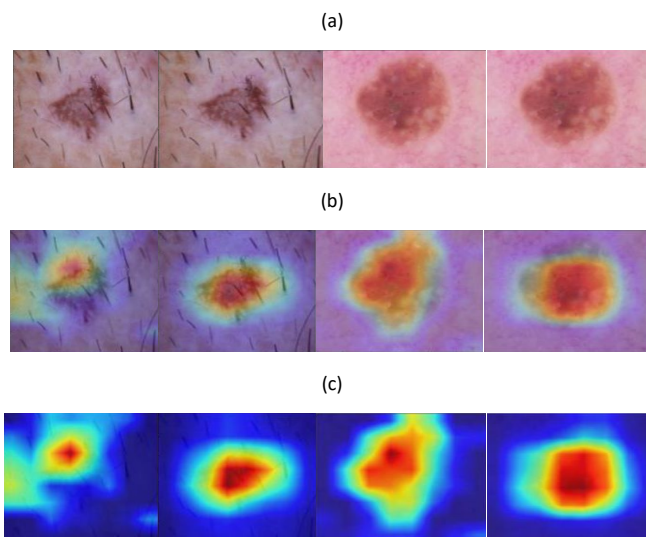


Fig. 18. Shows the combination of EfficientNet-B4 with SegNet, BOO, and SAttNet in the case of dermatological malignancy detection using randomly collected specimens from the test set from multiple datasets. (a) shows the clean dermoscopic input image, (b) shows the lesion segmentation using the MOO algorithm, and (c) shows a Grad-CAM heatmap showing the most diagnostically salient parts of the lesion, where red parts are areas of a higher diagnostic relevance.

of 99.656%. When compared to Meta-XPFL with XAI (Serhani, M. A. et al. 2025), the proposed method shows 5.46% gain. Compared to ViT+CustomCNN+Xception+Grad-CAM (Ali, A. et al. 2025) with 96.7%, there is 2.96% increase, while it shows 7.16% improvement over LIME+Grad-CAM (Garg, P. et al. 2025), which achieved 92.5%. For MSID dataset, EfficientNetB7+Grad-CAM (Kumar Saha, D. et al. 2025) achieved 98.8% accuracy, the proposed model managed to outperform slightly with 99.685%, shows 0.89% improvement. Fig. 18 illustrates the outputs of the EfficientNet-B4+SegNet+BOO+SAttNet model on random test samples from the datasets. The Grad-CAM visualization overlays heatmap that pinpoint critical areas within the lesion, with the most significant regions marked in red, confirming the model's focus on clinically relevant features. The SHAP summary violin plot (Fig. 19) provides a broad summary of how the different features contribute to the predictions of the model through the ISIC 2020 dataset. The following LIME analysis can further explain the single prediction instances by perturbing pixel values and discovering localized feature attentiveness, thus affording fine-scale interpretability as illustrated

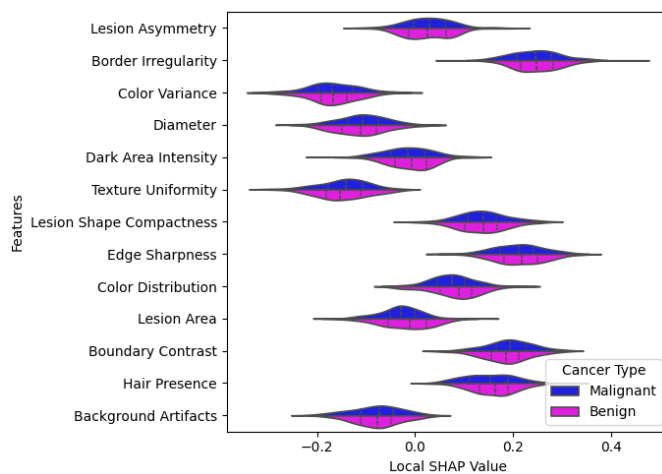


Fig. 19. SHAP summary violin plot illustrating the distribution and contribution magnitude of local SHAP values across key features in the ISIC 2020 dataset for skin cancer classification.

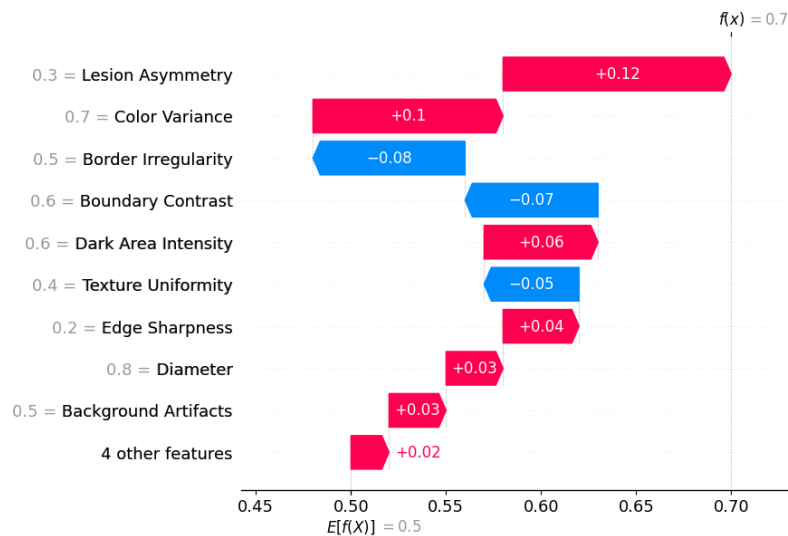


Fig. 20. Comparative feature importance analysis using LIME visualization for selected prediction instances.

Table 6.

Ablation study results showing the contribution of individual components in the proposed model (ISIC 2019 dataset).

Model configuration	AUC (%)	MCC	Kappa	Computation time (s)	Model complexity (FLOPs ×10 ⁹)
EfficientNet-B0 + UNet	96.257	0.921	0.908	128.473	9.836
EfficientNet-B4 + UNet	97.583	0.936	0.924	119.726	8.954
EfficientNet-B4 + SegNet	98.204	0.948	0.933	112.537	8.123
EfficientNet-B4 + SegNet + BOO	99.031	0.961	0.948	96.384	7.489
EfficientNet-B4 + SegNet + SAttNet	99.218	0.969	0.955	88.571	7.276
EfficientNet-B4 + SegNet + BOO + SAttNet	99.683	0.982	0.972	79.438	6.852
EfficientNet-B7 + SegNet + BOO + SAttNet	99.711	0.983	0.973	82.276	8.637
EfficientNet-B4 + UNet + BOO + SAttNet	99.537	0.979	0.968	86.749	7.193

in Fig. 20. Together with the advanced methods of explainability, EfficientNet-B4, SegNet, BOO, and SAttNet are integrated to produce a strong, transparent, and clinically meaningful primary diagnosis and precise analysis tool of skin cancer.

The ablation experiment in Table 6 shows the effectiveness of each of the constituents in enhancing model performance. The architecture that included EfficientNet-B4, SegNet, BOO, and SAttNet had the best area under the curve (AUC) of 99.683% which was 3.56% greater than that of the base model and 1.506 times greater than the SegNet-only model. The Matthews’s correlation coefficient (MCC) and Kappa value were improved by 6.63% which highlights better predictive consistency. Efficiency was gained by minimizing computational time by 38.18% and the model complexity by 30.32%. Its advantages are due to the capability of BOO to optimize feature selection based on the adaptive feature and spatial attention mechanisms of SAttNet, which jointly enhance image feature selection accuracy, convergence rate, and interpretability of models, leading to a strong and computationally efficient diagnostic system.

6. Conclusions

This work proposed XAI with optimized encoder-decoder architecture to help accurately diagnose skin cancer and make clinical decisions. The assessment of the model on a set of datasets, i.e. ISIC 2018-2020 and HAM10000, proves that it consists of pre-trained backbone networks (ResNet50 and EfficientNet-B4) and specific decoder modules (UNet and SegNet) to be used to perform lesion segmentation and classification. The BOO algorithm is utilized to be effective in the selection of relevant features to minimize computational overhead. A SAttNet is added to hone the focus on lesion boundaries, and therefore, increase prediction strength. In order to be interpretable and enable clinical trust, the framework embraces XAI methods, such as Grad-CAM, SHAP, and LIME, to offer both visual

and quantitative interpretations of model decisions, thus simplifying the provision of reliable assistance in diagnosis. The results show that the proposed EfficientNet-B4+SegNet+BOO+SAttNet model outperforms current state-of-the-art applications significantly in various benchmark datasets. Notable increases in accuracy are achieved with the model, including 0.89% percent on ISIC 2018 and 12.12% on ISIC 2019, versus the bests of competitors by up to 7.11% and 8.33% respectively. The model achieves an accuracy of 99.656% on the HAM10000 dataset and achieves an improvement of 13.68% on previous methods. Cross-layered XAI functions are utilized to facilitate explainability and interpretability: Grad-CAM provides human intuitive heatmap with priorities in the key areas of the lesion; SHAP provides the extent to which a particular feature contributes to the predictions; and LIME provides local and patient-specific explanations. Although such optimistic results exist, there are some limitations that should be taken into consideration. Although the synthetic augmentation reduces the issue of class imbalance, it might not be adequate to address the issues of rare lesions. The computational requirements of the proposed framework are a big challenge during the implementation in resource-intensive environments. Future studies ought to primarily focus on the assessment of large, multi-institutional cohorts of patients that combine multimodal data, and study the application of lightweight federated learning architecture to improve scalability, privacy protection, and operational clinical benefits.

CRedit authorship contribution statement

Mudassir Khan: Conceptualization, methodology, data curation, writing and editing. **Sai Bhuvana Kurada:** Literature survey, supervision, conceptualization. **Alaa Menshawi:** Methodology, supervision, project administration and writing. **Varun Malik:** Validation, literature survey, supervision and conceptualization. **Meteb Altaf:** Data interpretation, methodology and supervision.

Declaration of competing interest

The authors declare that they have no known competing financial interests or personal relationships that could have appeared to influence the work reported in this paper.

Data availability

The datasets used and/or analysed during the current study available from the corresponding author on reasonable request.

Declaration of generative AI and AI-assisted technologies in the writing process

The authors confirm that there was no use of artificial intelligence (AI)-assisted technology for assisting in the writing or editing of the manuscript, and no images were manipulated using AI.

Acknowledgment

The authors extend their appreciation to the Deanship of Research and Graduate Studies at King Khalid University for funding this work through Large Research Project under grant number RGP2/164/46.

Funding

This research work was funded by King Khalid University, Saudi Arabia.

References

- Abbas, S., Ahmed, F., Khan, W.A., Ahmad, M., Khan, M.A., Ghazal, T.M., 2025. Intelligent skin disease prediction system using transfer learning and explainable artificial intelligence. *Sci Rep* 15, 1746. <https://doi.org/10.1038/s41598-024-83966-4>
- AbuAlkebash, H., Saleh, R.A.A., Ertunç, H.M., 2025. Automated explainable deep learning framework for multiclass skin cancer detection and classification using hybrid YOLOv8 and vision transformer (ViT). *Biomed Signal Process Control* 108, 107934. <https://doi.org/10.1016/j.bspc.2025.107934>
- Ahmad, I., Alsulami, B.S., Alqurashi, F., 2024. Enhancing skin cancer detection with transfer learning and vision transformers. *IJACSA* 15 pp. 1027-1036. <https://doi.org/10.14569/ijacsa.2024.01510104>
- Akilandasowmya, G., Nirmaladevi, G., Sughanthi, S.U., Aishwariya, A., 2024. Skin cancer diagnosis: Leveraging deep hidden features and ensemble classifiers for early detection and classification. *Biomed Signal Process Control* 88, 105306. <https://doi.org/10.1016/j.bspc.2023.105306>
- Akter, M., Khatun, R., Talukder, M.A., Islam, M.M., Uddin, M.A., Ahamed, M.K.U., Khraisat, A., 2025. An integrated deep learning model for skin cancer detection using hybrid feature fusion technique. *Biomed Mater Devices* 3, 1433-1447. <https://doi.org/10.1007/s44174-024-00264-3>
- Ali, M.S., Miah, M.S., Haque, J., Rahman, M.M., Islam, M.K., 2021. An enhanced technique of skin cancer classification using deep convolutional neural network with transfer learning models. *Machine Learning with Applications* 5, 100036. <https://doi.org/10.1016/j.mlwa.2021.100036>
- Ali, A., Shahbaz, H., Damaševičius, R., 2025. xCViT: Improved vision transformer network with fusion of CNN and Xception for skin disease recognition with explainable AI. *Computers. Materials Continua* 83, 1367-1398. <https://doi.org/10.32604/cmc.2025.059301>
- Al-Rasheed, A., Ksibi, A., Ayadi, M., Alzahrani, A.I.A., Zakariah, M., Ali Hakami, N., 2022. An ensemble of transfer learning models for the prediction of skin cancers with conditional generative adversarial networks. *Diagnostics (Basel)* 12, 3145. <https://doi.org/10.3390/diagnostics12123145>
- Altman, N.S., 1992. An introduction to kernel and nearest-neighbor nonparametric regression. *Am Stat* 46, 175-185. <https://doi.org/10.1080/00031305.1992.10475879>
- Chakkarapani, V., Poornapushpakala, S. & Suresh, S. Enhancing Skin Cancer Detection with Multimodal Data Integration: A Combined Approach Using Images and Clinical Notes. *SN COMPUT. SCI.* 6, 72 (2025). <https://doi.org/10.1007/s42979-024-03601-x>
- Chanda, T., Haggenuellner, S., Bucher, T.C., Holland-Letz, T., Kittler, H., Tschandl, P., Heppt, M.V., Berking, C., Utikal, J.S., Schilling, B., Buerger, C., Navarrete-Dechent, C., Goebeler, M., Kather, J.N., Schneider, C.V., Durani, B., Durani, H., Jansen, M., Wacker, J., Wacker, J., Brinker, T.J., 2025. Dermatologist-like explainable AI enhances melanoma diagnosis accuracy: Eye-tracking study. *Nat Commun* 16, 4739. <https://doi.org/10.1038/s41467-025-59532-5>
- Das, A., Mohanty, M.N., 2025. Design of stacked ensemble classifier for skin cancer detection. *Multimedia Tools Applications* 1-20. <https://doi.org/10.1007/s11042-025-20630-7>
- Ennab, M., Mcheick, H., 2025. Advancing AI interpretability in medical imaging: A comparative analysis of pixel-level interpretability and grad-CAM models. *MAKE* 7, 12. <https://doi.org/10.3390/make7010012>
- Evans, H., Sivakumar, N., Bhandari, S., Graham, S., Snead, D., Patel, A., Robinson, A., 2025. Evaluating the pathological and clinical implications of errors made by an artificial intelligence colon biopsy screening tool. *BMJ Open Gastroenterol* 12, e001649. <https://doi.org/10.1136/bmjgast-2024-001649>
- Firasari, E., Khasanah, N., Cahyanti, F.L.D., Kholifah, D.N., Khultsum, U., Sarasati, F., 2024. Performance evaluation of ResNet50 and MobileNetV2 in skin cancer image classification with various optimizers. 2024 International Conference on Information Technology Research and Innovation (ICITRI) Jakarta, Indonesia, pp. 376-380. <https://doi.org/10.1109/icitri62858.2024.10698943>
- Garg, P., Sharma, M.K., Kumar, P., 2025. Transparency in diagnosis: Unveiling the power of deep learning and explainable AI for medical image interpretation. *Arab J Sci Eng* 50, 15751-15767. <https://doi.org/10.1007/s13369-024-09896-5>
- Gupta, R.K., 2025. Interpretable AI-enabled model for skin cancer diagnosis using LIME. *Procedia Computer Sci* 260, 3-11. <https://doi.org/10.1016/j.procs.2025.03.171>
- Halbers, L.P., Cole, K.H., Ng, K.K., Fuller, E.B., Chan, C.E.T., Callicotat, C., Metcalfe, M., Chen, C.C., Barhoosh, A.A., Reid-McLaughlin, E., Kent, A.D., Torrey, Z.R., Steward, O., Luptak, A., Prescher, J.A., 2024. A modular platform for bioluminescent RNA tracking. *Nat Commun* 15, 9992. <https://doi.org/10.1038/s41467-024-54263-5>
- Hu, B., Zhou, P., Yu, H., Dai, Y., Wang, M., Tan, S., Sun, Y., 2024. LeaNet: Lightweight U-shaped architecture for high-performance skin cancer image segmentation. *Comput Biol Med* 169, 107919. <https://doi.org/10.1016/j.combiomed.2024.107919>
- Ieracitano, C., Morabito, F.C., Hussain, A., Suffian, M., Mammone, N., 2025. TixAI: A trustworthiness index for explainable AI in skin lesions classification. *Neurocomputing* 630, 129701. <https://doi.org/10.1016/j.neucom.2025.129701>
- ISSN 2640-4567 eISSN2640-4567 Received 31 May 2024 Revised 31 August 2024 Pages n/a - n/a <https://advanced.onlinelibrary.wiley.com/doi/epdf/10.1002/aisy.202400438>
- Kavitha, C., Priyanka, S., Kumar, M.P., Kusuma, V., 2024. Skin cancer detection and classification using deep learning techniques. *Procedia Computer Sci* 235, 2793-2802. <https://doi.org/10.1016/j.procs.2024.04.264>
- Kumar, K.A. Vanmathi, C., 2024. Segmentation and detection of skin cancer using fuzzy cognitive map and deep Seg Net. *Soft Computing* 28, 4575-4592. <https://doi.org/10.1007/s00500-024-09644-9>
- Kibriya, H., Siddiqa, A., Khan, W.Z., 2025. Melanoma lesion localization using UNet and explainable AI. *Neural Comput & Applic* 37, 10175-10196. <https://doi.org/10.1007/s00521-025-11080-1>
- Kumar, K.A., Vanmathi, C., 2025. A hybrid parallel convolutional spiking neural network for enhanced skin cancer detection. *Sci Rep* 15, 11137. <https://doi.org/10.1038/s41598-025-85627-6>
- Kumar Saha, D., Rafi, S., Mridha, M.F., Alfarhood, S., Safran, M., Kabir, M.M., Dey, N., 2025. Mpox-XDE: An ensemble model utilizing deep CNN and explainable AI for monkeypox detection and classification. *BMC Infect Dis* 25, 403. <https://doi.org/10.1186/s12879-025-10811-y>
- Mahmud, M.Z., Reza, M.S., Alve, S.R., Islam, S. Fahmid, N., 2024. Advance transfer learning approach for identification of multiclass skin disease with LIME explainable AI technique. *medRxiv*, pp.2024-12. <https://doi.org/10.1101/2024.12.02.24318311>
- Na, A. 2025. Identification improvement of malignant skin diseases for diverse skin tones with grad-CAM. In: *Lecture notes in computer science, Pattern recognition. ICPR 2024 International workshops and challenges Lecture notes in computer science, Pattern recognition. ICPR 2024 International workshops and challenges (Cham: Springer Nature Switzerland)*, pp. 129-140. https://doi.org/10.1007/978-3-031-87666-8_10
- Narayanan, V.S., Sikha, O.K., Benitez, R., 2024. IARS SegNet: Interpretable attention residual skip connection SegNet for melanoma segmentation. *IEEE Access* 12, 126122-126134. <https://doi.org/10.1109/access.2024.3404224>
- Nawaz, K., Zaniab, A., Shabir, I., Li, J., Wang, Y., Mahmood, T., Rehman, A., 2025. Skin cancer detection using dermoscopic images with convolutional neural network. *Sci Rep* 15, 7252. <https://doi.org/10.1038/s41598-025-91446-6>
- Noor, A.A., Manzoor, A., MazharQureshi, M.D., Qureshi, M.A., Rashwan, W., 2025. Unveiling explainable AI in healthcare: Current trends, challenges, and future directions. *Wiley Interdiscip Rev: Data Min Knowl Discov* 15, e70018. <https://doi.org/10.1002/widm.70018>
- Qadrie, Zulfiqar, Maqbool, Mudasar, Dar, Mohd Altaf and Qadir, Afshana. "Navigating challenges and maximizing potential: Handling complications and constraints in minimally invasive surgery" *Open Health*, vol. 6, no. 1, 2025, pp. 20250059. <https://doi.org/10.1515/ohe-2025-0059>
- Qin, X., Lin, M., Lai, Z., Mo, J., Wen, S., Yang, X., 2024. The fluorescent and bioluminescent probes for detecting hydrazine in recent years. *Dyes Pigm* 231, 112378. <https://doi.org/10.1016/j.dyepig.2024.112378>
- Rashid, M., Sharma, M., 2025. AI-assisted diagnosis and treatment planning—A discussion of how AI can assist healthcare professionals in making more accurate diagnoses and treatment plans for diseases. *AI in disease detection: Advancements Applications* 313-336. <https://doi.org/10.1002/9781394278695.ch14>
- Reddy, A.S., M.P. G., 2025. Skin cancer detection using optimized mask r-CNN and two-fold-deep-learning-classifier framework. *Multimed Tools Appl* 84, 36871-36898. <https://doi.org/10.1007/s11042-024-20377-7>
- Ronzetti, M., Simeonov, A., 2025. A comprehensive update on the application of high-throughput fluorescence imaging for novel drug discovery. *Expert Opin Drug Discov* 20, 785-797. <https://doi.org/10.1080/17460441.2025.2499123>
- Sargunan, I., Maram, B., Rajan, C., Prasad, V., Balasubramaniam, S.R., Gnanasekaran, D., 2025. Discrete neighborhood difference pattern-based feature extraction and hybrid deep learning model for melanoma skin cancer detection. *Biomed Signal Process Control* 107, 107812. <https://doi.org/10.1016/j.bspc.2025.107812>
- Serhani, M.A., Tariq, A., Qayyum, T., Taleb, I., Din, I., Trabelsi, Z., 2025. Meta-XPFL: An explainable and personalized federated meta-learning framework for privacy-aware IoMT. *IEEE Internet Things J* 12, 13790-13805. <https://doi.org/10.1109/jit.2025.3541844>

- Shah, S.A.H., Shah, S.T.H., Khaled, R., Buccoliero, A., Shah, S.B.H., Di Terlizzi, A., Di Benedetto, G., Deriu, M.A., 2024. Explainable AI-based skin cancer detection using CNN, particle swarm optimization and machine learning. *J Imaging* 10, 332. <https://doi.org/10.3390/jimaging10120332>
- Shoughi, A., Dowlatshahi, M.B., Amiri, A., 2025. New challenges and opportunities to explainable artificial intelligence (XAI) in smart healthcare. In: *Explainable AI in healthcare imaging for medical diagnoses* (Explainable AI in healthcare imaging for medical diagnoses: Elsevier), pp. 503-527. <https://doi.org/10.1016/b978-0-443-23979-3.00020-8>
- Swapno, S.M.M.R., Nobel, S.M.N., Meena, P.K., Meena, V.P., Bahadur, J., Appaji, A., 2025. Accelerated and precise skin cancer detection through an enhanced machine learning pipeline for improved diagnostic accuracy. *Results Eng* 25, 104168. <https://doi.org/10.1016/j.rineng.2025.104168>
- Tauhid Dinitra, N., Wijayanto, I., Akhyar, F., Sekar Safitri, A., Satria Firdhaust, R., 2024. Enhancing skin cancer classification using efficientNet-based architectures. 2024 International Conference on Data Science and Its Applications (ICoDSA) Kuta, Bali, Indonesia, pp. 415-420. <https://doi.org/10.1109/icodsa62899.2024.10652183>
- Thanga Purni, J.S., Vedhapriyavadhana, R., 2024. EOSA-Net: A deep learning framework for enhanced multi-class skin cancer classification using optimized convolutional neural networks. *J Saud Univ - Computer Inf Sci* 36, 102007. <https://doi.org/10.1016/j.jksuci.2024.102007>
- Verma, A., Kaur, P., 2025. Classifying tomato leaf diseases using diverse deep learning architectures: AlexNet, DenseNet, Inception, Xception. In 2025 IEEE International Conference on Interdisciplinary Approaches in Technology and Management for Social Innovation (IATMSI) 3, 1-6. IEEE. <https://doi.org/10.1109/IATMSI64286.2025.10984581>
- Verma, N., Ranvijay & Yadav, D.K., 2025. A comprehensive review on step-based skin cancer detection using machine learning and deep learning methods. *Arch Computat Methods Eng* 32, 4359-4412. <https://doi.org/10.1007/s11831-025-10275-y>
- Vibha, T.R., Saravanan, C., Divya, T.L., 2025. Melanoma skin cancer detection and classification using deep learning and image processing. *SN Comput Sci* 6. <https://doi.org/10.1007/s42979-025-04009-x>
- Vineet Kumar Dubey, Apoorva Sharma, Vandana Dixit Kaushik, Skin Lesion Identification Using Carpet Weaving Fossa Algorithm based Convolutional Neural Network with Transfer Learning and Tversky Loss-U-Net++ Based Segmentation, *Neurocomputing*, 2026, 132587, ZSSN 0925-2312, <https://doi.org/10.1016/j.neucom.2025.132587>.
- Wu, Y., Hao, C., Gao, C., Hageman, M., Lee, S., Kirkland, T.A., Gray, N.S., Su, Y., Lin, M.Z., 2025. Pharmacodynamics of Akt drugs revealed by a kinase-modulated bioluminescent indicator. *Nat Chem Biol* 21, 1194-1204. <https://doi.org/10.1038/s41589-025-01846-y>